Probabilistic Failure Criterion of SiC/SiC Composites Under Multiaxial Loading

FINAL REPORT

Jia-Liang Le[1], Joseph F. Labuz[2], Chen Hu[3], and Takaaki Koyanagi[4]

SUMMARY: Owing to its excellent mechanical properties and stability under high temperature and neutron irradiation conditions, SiC/SiC composites have emerged as a promising material for light water reactors (LWRs) in the development of accident-tolerant fuel (ATF) systems. Structural integrity and retention of hermeticity are two crucial requirements for SiC/SiC claddings during normal operations, and both of them are closely related to the proportional limit stress (PLS) of the material. Understanding the behavior of SiC/SiC composites under multi-axial stress states and developing a probabilistic approach for evaluating the structural vulnerability are of paramount importance for reliability-based analysis and design of SiC/SiC composite claddings. So far, there has been very limited effort towards experimental and analytical investigations of probabilistic failure of SiC/SiC claddings. This critical knowledge gap motivates this research.

A probabilistic failure criterion for SiC/SiC composites under multi-axial loading is developed, and this criterion is incorporated into reliability analysis of the structural integrity of SiC/SiC fuel cladding. The research consists of two parts: 1) experimental investigation of multiaxial failure behavior of SiC/SiC composites, and 2) theoretical modeling of time-dependent probabilistic failure of SiC/SiC cladding. In the experimental investigation, the PLS is determined through the examination of stress-strain response, the acoustic emission measurement, as well as the X-ray computed tomography. The theoretical framework is derived by combining the finite weakest-link statistical model and the subcritical damage growth model. This theoretical model captures the time-dependent failure mechanism of the material, which has a major consequence for predicting the lifetime distribution of the cladding. Meanwhile, the model also predicts that the failure statistics of the cladding depends strongly on the cladding length.

The results of the multiaxial experiments reveal the level of statistical variation of the PLS of SiC/SiC materials under different stress states. The theoretical model provides a robust analytical tool for extrapolation of small-scale laboratory test results to the behavior of full-scale claddings. These findings establish a scientific foundation for the development of reliability-based design of SiC/SiC fuel claddings, which will play an essential role in improving the structural safety and integrity of LWRs.

[1]Department of Civil, Environmental, and Geo- Engineering, University of Minnesota
[2]Department of Civil, Environmental, and Geo- Engineering, University of Minnesota
[3]Department of Civil, Environmental, and Geo- Engineering, University of Minnesota
[4]Material Science and Technology Division, Oak Ridge National Laboratory

Contents

List of Tables

List of Figures

1 Introduction

The 2011 Fukushima Daiichi nuclear power plant accident has stimulated the active development of accident-tolerant fuels (ATFs) and accident-tolerant cores [31]. In recent years, silicon carbide (SiC) fiber-reinforced SiC matrix (SiC/SiC) composites have attracted increasing attention as an alternative material for fuel cladding in light water reactors (LWRs) [16]. Extensive experimental research showed that the SiC/SiC composites can retain excellent mechanical properties under high temperature and neutron irradiation conditions. Compared to traditional zirconium alloy cladding and core, which would produce explosive hydrogen in a water vapor environment, SiC/SiC composites exhibit general chemical inertness at very high temperatures [30]. Moreover, they are also stable under high-dose neutron [16]. Owing to these attractive features, SiC/SiC composites are considered favorably for providing passive safety for LWRs in beyond-design-basis severe accident scenarios [31].

For LWR fuel claddings, SiC/SiC composites are fabricated in the form of long tubes. Considerable efforts have been devoted towards experimental investigations of SiC/SiC composite tubes under different loading scenarios including uniaxial tension, hoop tension, and multiaxial loading [7, 27, 8, 24, 26]. It is generally observed that the specimen would exhibit a linear elastic behavior up to a stress level referred to as the proportional limit stress (PLS). Upon reaching the PLS, the matrix material experiences notable damage and the specimen shows a reduction of stiffness. As damage accumulates in the matrix, the fibers start to take more loading. This eventually leads to localized fiber breakage, and the specimen attains its ultimate tensile strength (UTS). For the purpose of cladding design, the PLS and UTS are two critical metrics. It is considered that the PLS indicates the stress level at which damage poses the risk of a gas release, whereas the UTS corresponds to the scenario that the structure loses its load capacity. One important observation made from a recent inter-laboratory round robin study is that the PLS and UTS of SiC/SiC composites exhibit a considerably level of variability. The measured the coefficients of variation of PLS and UTS are 9.7% and 12.5%, respectively [27].

Despite the aforementioned experimental efforts, only one study has reported the failure surface of SiC/SiC composites under multiaxial loading [7]. Procedures for uniaxial and hoop tensile tests for SiC/SiC composites have been well established (ASTM C1275 and ASTM C1819). So far, limited efforts have been devoted to multiaxial loading. Furthermore, for hoop tensile tests the current test method relies on elastomeric inserts [26]. However, friction between the elastomeric insert and the internal surface of the specimen may cause unpredictable shear stresses, which affect the measurement of material strength parameters. Therefore, a more robust and reliable testing system is needed.

The statistical nature of PLS and UTS of SiC/SiC composites can be attributed to the heterogeneity of the material. In the manufacturing process, the SiC matrix is deposited from gaseous reactants onto a heated substrate of fibrous preforms of SiC [18]. This process, called

chemical vapor infiltration (CVI), inevitably introduces internal pores in the matrix. It is reported that the porosity of SiC/SiC composites is 8-17% [17, 7]. Computed X-ray tomography showed that the large pores between fiber tows are crucial to damage development compared to small pores [25]. The size and location of these internal pores are affected by fiber architecture and kinetics of deposition. The uncertainty in the manufacturing process leads to statistical variation in both the local stress field and material resistance and consequently the macroscopically observed variability in PLS and UTS.

The observed variability of PLS and UTS has important implications for design of SiC/SiC composite claddings. It is widely acknowledged that engineering structures must be designed against an acceptable risk level. In the current design approach, an empirical reduction factor is applied to the PLS to account for its uncertainty [22]. This concept is similar to safety factors used in design of concrete and steel structures. Safety factors allow us to perform reliability-based structural design through deterministic analysis. The essential step is to relate the safety factors to the failure risk of the structure [13, 19, 2]. Evidently this relation must be derived from a probabilistic model of structural failure.

In recent years, considerable attention has been directed towards investigation of the failure statistics of SiC/SiC composites. Previous studies have largely used the two-parameter Weibull distribution for the probability distributions of PLS and UTS [27, 29, 9]. The Weibull distribution belongs to the class of extreme value statistics [33, 34, 32, 2], which indicates that the failure statistics of the structure can be represented by an infinite weakest-link model. Physically it implies that a damage localization mechanism occurs and that the structure must be much larger than the size of the damage zone. A series of recent studies discussed the applicability of the Weibull distribution for strength statistics of structures made of quasibrittle materials, such as composites and ceramics, which feature a strain softening behavior and damage localization mechanism [5, 3, 21, 2]. It was shown that, for most quasibrittle structures, the structure size is not sufficiently large to guarantee the validity of the Weibull distribution. The same issue also applies to SiC/SiC composite tubes. While the full length cladding is 4m long, the laboratory test specimen is less than 100 mm, which is not significantly larger than the size of the damage zone. Therefore, the classical Weibull model cannot be used to extrapolate the laboratory test result to full-scale cladding design.

In addition to the inapplicability of the Weibull distribution for design extrapolation, probabilistic modeling of SiC/SiC composite tubes is further complicated by the time evolution of the internal stress state. A thermomechanical analysis was recently performed to investigate the stress history of the SiC/SiC cladding over its service lifetime [6, 28]. It was shown that the cladding experiences a complicated stress history along axial and hoop directions in LWRs. To model the lifetime of the cladding, it is crucial to take into account the damage accumulation mechanism. The failure probability of the entire structure at the present time depends not only on the current stress state but also on the prior loading history. So far, such a time-dependent

behavior has not been investigated.

In this study, we develop a probabilistic failure criterion for SiC/SiC composites under multiaxial loading, and incorporate the criterion into reliability analysis of the structural integrity of SiC/SiC fuel cladding. The research consists of two parts: 1) experimental investigation of multiaxial failure behavior of SiC/SiC composites, and 2) theoretical modeling of time-dependent probabilistic failure of SiC/SiC cladding. In the experimental investigation, the PLS is determined through the examination of stress-strain response and the acoustic emission measurement. The theoretical framework is derived by combining the finite weakest-link statistical model and the subcritical damage growth model. This theoretical model captures the time-dependent failure mechanism of the material, which has a major consequence for predicting the lifetime distribution of the cladding. Meanwhile, the model also predicts that the failure statistics of the cladding depends strongly on the cladding length. The results of the multiaxial experiments reveal the level of statistical variation of the PLS of SiC/SiC materials under different stress states. The theoretical model provides a robust analytical tool for extrapolation of small-scale laboratory test results to the behavior of full-scale claddings. These findings lay down a scientific foundation for the development of reliability-based design of SiC/SiC fuel claddings, which will play an essential role in improving the structural safety and integrity of LWRs.

2 Probabilistic Time-Dependent Failure Model

This chapter presents a new stress-based multiaxial failure model for the PLS of SiC/SiC materials. The model is further extended to predict the specimen lifetime through a damage kinetics model. By considering the PLS under uniaxial tension in hoop and axial directions as well as biaxial loading as random variables, the model can be used to calculate the probability distribution of specimen lifetime.

2.1 Stress-based failure criterion

Consider a laboratory test specimen under general loading (axial load F, internal pressure p, and torsion T), as shown in Fig. 2.1. To discuss the failure criterion, we first need to define the meaning of failure. For structural design, failure often refers to the attainment of the peak load capacity. At that point, the structure would fail under controlled load. For most structures, as the peak load is reached, the material has already experienced some degree of damage. For fuel claddings, failure can be defined as the damage initiation, which could lead to leakage of fission gas. This is not a structural failure but it could cause severe safety consequence of the LWR. In this study, we define the material failure as damage initiation, which is more stringent than the strength-based failure criterion.

For damage initiation, it suffices to adopt a stress-based failure criterion. To formulate such a criterion, we first define the following nominal stresses:

$$\sigma_{\theta\theta} = \frac{r_i^2(r_m^2 + r_e^2)}{r_m^2(r_e^2 - r_i^2)}p \tag{2.1}$$

$$\sigma_{zz} = \frac{F + p\pi r_i^2}{\pi(r_e^2 - r_i^2)} \tag{2.2}$$

$$\sigma_{z\theta} = \frac{3T}{2\pi(r_e^3 - r_i^3)} \tag{2.3}$$

where $r_i,\ r_e$ are the inner and outer radius of the specimen, respectively, and $r_m = 0.5(r_i + r_e)$. While these nominal stresses serve as load parameters in the dimension of stress, they physically represent the homogenous elastic stresses of the test specimen.

Bernachy-Barbe et al. proposed the following strength-based failure criterion [7]:

$$F(\sigma_i, k_i) = k_1\langle\sigma_1\rangle^2 + k_1\langle\sigma_2\rangle^2 + k_2\langle\sigma_1\rangle\langle\sigma_2\rangle + k_3\sigma_3^2 - 1 \geq 0 \tag{2.4}$$

where σ_1, σ_2 = in-plane principal elastic stresses, $\sigma_3 = \sigma_{\theta\theta} - \sigma_{zz}$, k_i $(i = 1, 2, 3)$ = model constants, and $\langle x\rangle$ = Macaulay bracket= $\max(x, 0)$. It was shown that this failure criterion can well capture the multiaxial failure behavior of SiC/SiC composites with $\pm 45°$ tow orientation [7]. The term $k_3\sigma_3^2$ corresponds to damage of tows oriented at $\pm 45°$. By considering some specific

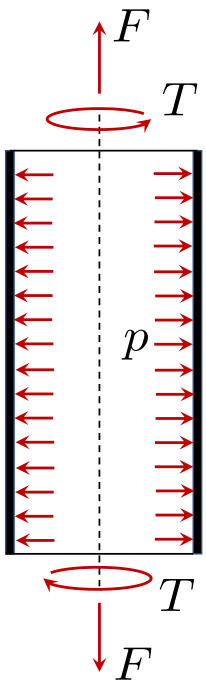

Figure 2.1: Schematic of loading configuration of SiC/SiC cladding.

loading scenarios, such as uniaxial tension, uniaxial compression, and equi-biaxial tension, we can express k_i's by

$$k_1 = \frac{1}{f_t^2} - \frac{1}{f_c^2}; \quad k_2 = \frac{1}{f_b^2} - 2k_1; \quad k_3 = \frac{1}{f_c^2} \tag{2.5}$$

where f_t, f_c and f_b denote the nominal strengths of the specimen corresponding to the uniaxial tensile, uniaxial compressive, and biaxial tensile stress states, respectively. It is clear that f_t, f_c and f_b corresponds to the aforementioned PLS. It is worthwhile to note that these nominal strengths are structural properties, which could vary with the specimen length [2]. Therefore, the failure criterion itself (Eq. 2.4) is dependent on the specimen length.

Note that in Eq. 2.4 the tensile strengths in the axial and hoop directions are the same. This may not be the case if the tows do not orient at $\pm 45°$. A more general failure criterion can be written by

$$F(\sigma_i) = \frac{\langle \sigma_{\theta\theta} \rangle^2}{f_{t\theta}^2} + \frac{\langle \sigma_{zz} \rangle^2}{f_{tz}^2} - \frac{\langle \sigma_{\theta\theta} \rangle \langle \sigma_{zz} \rangle}{f_0^2} + \frac{\sigma_{\theta z}^2}{f_\tau^2} - 1 \geq 0 \tag{2.6}$$

where $f_{t\theta}$ = tensile strength in the hoop direction, f_{tz} = tensile strength in the axial direction, f_τ = shear strength, and f_0 can be related to the biaxial strength f_b by considering a biaxial test $\sigma_{\theta\theta} = \sigma_{zz} = f_b$, which gives

$$f_0 = (f_{t\theta}^{-2} + f_{tz}^{-2} - f_b^{-2})^{-1/2} \tag{2.7}$$

In the study, we will use Eq. 2.6 for describing the failure surface corresponding to PLS. Furthermore, the recent thermo-mechanical elastic analysis of SiC/SiC cladding under a combination of external pressure, internal pressure, temperature, and irradiation-induced swelling showed that the shear stress $\sigma_{\theta z}$ is insignificant as compared to the axial and hoop stresses [28]. Therefore, we may ignore the shear component in Eq. 2.6, and the failure criterion becomes:

$$F(\sigma_i) = \frac{\langle\sigma_{\theta\theta}\rangle^2}{f_{t\theta}^2} + \frac{\langle\sigma_{zz}\rangle^2}{f_{tz}^2} - \frac{\langle\sigma_{\theta\theta}\rangle\langle\sigma_{zz}\rangle}{f_0^2} - 1 \geq 0 \tag{2.8}$$

Due to the inherent material inhomogeneity, $f_{t\theta}$, f_{tz}, and f_b would exhibit a certain degree of variability. Therefore, they should be considered as random variables. Consequently, the failure probability of the test specimen under given loading can be expressed by

$$\begin{aligned} P_f(\sigma_i) &= 1 - \Pr[F(\sigma_i, f_{t\theta}, f_{tz}, f_b) \leq 0] & (2.9)\\ &= 1 - \iiint_\Omega f(x_1, x_2, x_3)\mathrm{d}x_1\mathrm{d}x_2\mathrm{d}x_3 & (2.10)\end{aligned}$$

where x_i $(i = 1, 2, 3)$ denote the random values of $f_{t\theta}$, f_{tz} and f_b, respectively, Ω denotes the region of $F(\sigma_i, f_{t\theta}, f_{tz}, f_b) \leq 0$, and $f(x_1, x_2, x_3)$ is the joint probability density function (pdf) of random variables $f_{t\theta}$, f_{tz}, and f_b. In general, the integral in Eq. 2.10 needs to be evaluated numerically.

2.2 Extension to time-dependent failure behavior

The foregoing analysis is anchored by a stress-based failure criterion. In actual applications, the SiC/SiC claddings are subjected to time-dependent loading, which is lower than the quasistatic load capacity. However, the material could still fail after a substantial period of loading due to subcritical damage growth. In this case, the key design parameter is the structural lifetime, or time-to-failure. Therefore, it is necessary to reformulate the failure criterion (Eq. 2.8) for calculating the structural lifetime.

To this end, we consider a damage kinetics model, through which the PLS can be related to the specimen lifetime. Following the framework of continuum damage mechanics [23, 14, 15], we introduce a damage parameter ω, which ranges from 0 (intact) to 1 (fully damaged). We propose the following kinetics model:

$$\frac{\mathrm{d}\omega}{\mathrm{d}t} = \frac{g^n(\sigma_i)\phi(\omega)}{\langle k - g(\sigma_i)\rangle^n} \tag{2.11}$$

where $g(\sigma) = f_{t\theta}^{-2}\langle\sigma_{\theta\theta}\rangle^2 + f_{tz}^{-2}\langle\sigma_{zz}\rangle^2 - f_0^{-2}\langle\sigma_{\theta\theta}\rangle\langle\sigma_{zz}\rangle$, and k, n are constants. In continuum damage mechanics, a typical choice is $\phi(\omega) = (1-\omega)^{-1}$. Eq. 2.11 is phenomenological in nature, but it reflects the following well-expected behaviors: 1) the damage growth rate is zero at the absence of stress; 2) the damage growth rate increases with the applied stress; and 3) the damage growth rate is non-negative, which signifies the fact that damage growth is irreversible.

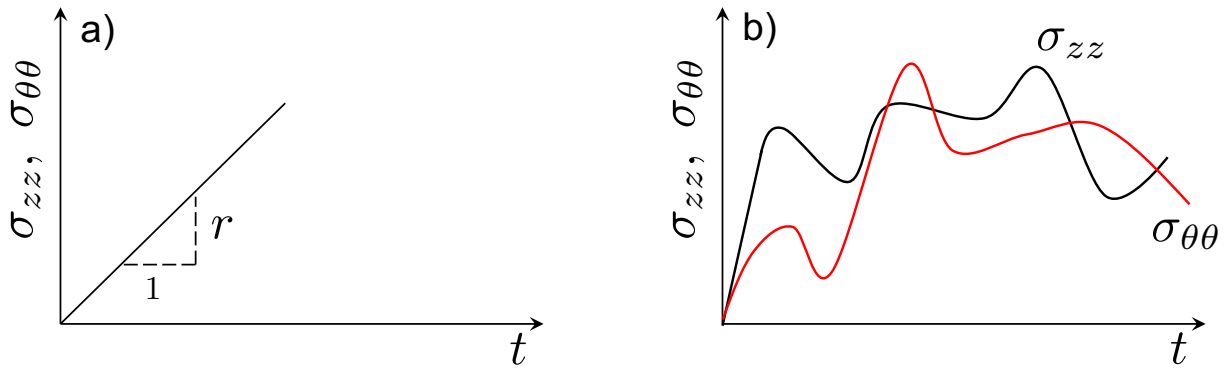

Figure 2.2: Loading protocols: a) reference ramped loading, and b) general loading history.

The damage kinetics model implies that the PLS would depend on the loading rate. Let r denote the loading rates used in the uniaxial tensile experiments in hoop and axial directions. These experiments directly measure $f_{t\theta}$ and f_{tz}. To relate the PLS to the specimen lifetime, we now consider two loading protocols: 1) reference linearly ramped loading and 2) general time-dependent loading, as shown in Fig. 2.2. For the reference linearly ramped loading, we consider the case of equi-biaxial loading, i.e. $\sigma_{\theta\theta} = \sigma_{zz} = rt$. By applying the separation of variables to Eq. 2.11, we have

$$\int_0^{\omega_c} \frac{\mathrm{d}\omega}{\phi(\omega)} = \int_0^{t_c} \frac{\alpha^n t^{2n} \mathrm{d}t}{(k - \alpha t^2)^n} \tag{2.12}$$

where $\alpha = r^2(f_{t\theta}^{-2} + f_{tz}^{-2} - f_0^{-2})$, ω_c = critical damage extent at which the specimen fails under load controlled test, and t_c = time to failure. Meanwhile, the stress-based failure criterion (Eq. 2.8) indicates $\alpha t_c^2 = 1$, or $t_c = \alpha^{-1/2}$. By substituting the expression of t_c into Eq. 2.12, we obtain

$$\int_0^{\omega_c} \frac{\mathrm{d}\omega}{\phi(\omega)} = C/\sqrt{\alpha} \tag{2.13}$$

where $C = \int_0^1 x^{2n}(k - x^2)^{-n}\mathrm{d}x$.

Now consider a general loading history $\sigma_i(t)$ $(i = 1 - 3)$. Applying the same analysis of the kinetics model to this general loading case yields

$$\int_0^{\omega_c} \frac{\mathrm{d}\omega}{\phi(\omega)} = \int_0^{t_f} \frac{\left\{f_{t\theta}^{-2}\langle\sigma_{\theta\theta}(t)\rangle^2 + f_{tz}^{-2}\langle\sigma_{zz}(t)\rangle^2 - f_0^{-2}\langle\sigma_{\theta\theta}(t)\rangle\langle\sigma_{zz}(t)\rangle\right\}^n}{\left\{k - \left[f_{t\theta}^{-2}\langle\sigma_{\theta\theta}(t)\rangle^2 + f_{tz}^{-2}\langle\sigma_{zz}(t)\rangle^2 - f_0^{-2}\langle\sigma_{\theta\theta}(t)\rangle\langle\sigma_{zz}(t)\rangle\right]\right\}^n}\mathrm{d}t \tag{2.14}$$

where t_f = failure time or the specimen lifetime. We further postulate that, for different loading paths, the specimen would fail at the same critical damage extent. By equating Eqs. 2.12 and 2.14, we obtain

$$\int_0^{t_f} \frac{\left\{f_{t\theta}^{-2}\langle\sigma_{\theta\theta}(t)\rangle^2 + f_{tz}^{-2}\langle\sigma_{zz}(t)\rangle^2 - f_0^{-2}\langle\sigma_{\theta\theta}(t)\rangle\langle\sigma_{zz}(t)\rangle\right\}^n}{\left\{k - \left[f_{t\theta}^{-2}\langle\sigma_{\theta\theta}(t)\rangle^2 + f_{tz}^{-2}\langle\sigma_{zz}(t)\rangle^2 - f_0^{-2}\langle\sigma_{\theta\theta}(t)\rangle\langle\sigma_{zz}(t)\rangle\right]\right\}^n} \mathrm{d}t = C/\sqrt{\alpha} \tag{2.15}$$

From Eq. 2.15, we can solve t_f for any given time-dependent loading. Note that, by using the equivalent damage, the actual form of $\phi(\omega)$ in Eq. 2.11 is not required here. If one wants to quantify the critical damage ω_c at failure, then $\phi(\omega)$ needs to be formulated. By considering $f_{t\theta}$, f_{tz} and f_b as random variables, we perform Monte Carlo simulation to determine the probability distribution of t_f (i.e. lifetime distribution) of the laboratory specimen for a given loading history. The algorithm for calculating this probability distribution is shown below. Note that the probability distribution of t_f exactly equals to the failure probability P_{fs} of the specimen at any given time t, i.e. $\Pr(t_f \leq t) = P_{fs}(t)$. What follows is that the failure probability of the specimen during a particular period of time ($t \in [t_1, t_2]$) can be calculated by $P_{fs} = P_{fs}(t_2) - P_{fs}(t_1)$.

Algorithm 1 Probabilistic Time-Dependent Failure Model Algorithm

for Every material element in simulation **do**
    Find its loading history $\boldsymbol{\sigma}(x,t)$
    Array $t_f\_array = [\,]$
    Monte Carlo sampling $f_{tz}, f_{t\theta}, f_b \sim Prob(\sigma_N)$
    for Every sampling of (f_t, f_b, f_c) **do**
        Calculate its corresponding k_1, k_2, k_3
        Solve t_f based on Eq. 2.15
        Append t_f in t_f_array
    end for
    Sort t_f_array
    Calculate P_{fs} based on sorted t_f_array
end for

3 Multiaxial Experiments on SiC/SiC Specimens

This chapter presents a robust multiaxial testing setup for SiC/SiC tubular specimens. By using this setup, multiaxial experiments with four loading paths were performed, and the failure surfaces for PLS and UTS were constructed. Meanwhile, new criteria for determining the PLS using both strain invariants and AE cumulative energy were developed.

3.1 Multiaxial testing apparatus and data acquisition system

The design of the new multiaxial test apparatus aims to facilitate different combinations of axial loading, internal fluid pressure, and external fluid pressure as shown in Fig. 2.1. Though the multiaxial loading configuration shown in Fig. 2.1 is seemingly simple, several practical problems must be solved to perform successful multiaxial tests. First of all, specimens must be carefully fabricated such that wall thickness should be uniform in circumferential and axial directions. General Atomics (GA) is capable of producing 1-m long tubes by using the CVI process with adequate straightness, wall thickness uniformity, roundness, and reproducibility of surface roughness [8]. For the present research, GA manufactured twenty-one 300-mm long tubes of SiC/SiC ceramic matrix composites with ±55° triaxial braided fiber orientation. The internal and outer diameters are 8mm±0.25mm and 10mm ±0.25mm. The tubes are cut with a diamond saw into specimens of length 72–73mm. The cut surface is carefully prepared such that it is smooth and no fibers are pulled out. Figure 3.1 shows a specimen and architecture observed by optical microscopy and scanning electron microscopy [27].

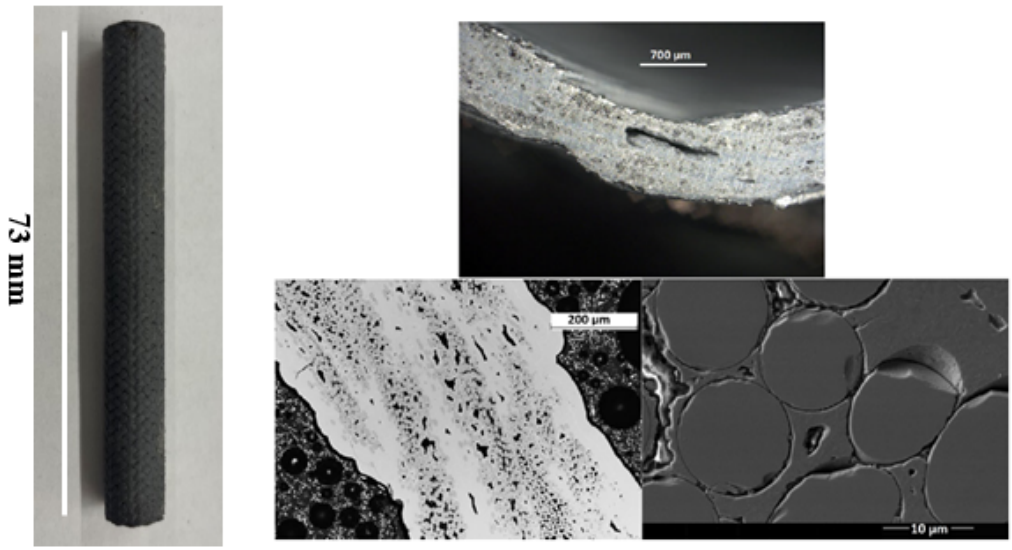

Figure 3.1: Specimen prepared and similar specimen observed by optical microscopy and scanning electron microscopy (right) [27].

A major issue in the design of the multiaxial apparatus is the effective isolation (jacketing)

from the internal fluid pressure. Since SiC/SiC composites inherently contain internal pores, sealing of the specimen is of critical importance. Due to the woven geometry of the specimen surface and tensile loading in the axial direction, it is challenging to directly seal the interface between the SiC/SiC specimen and loading apparatus. It has been proposed to use polyurethane coatings or high-strength epoxy to seal the interface and transmit axial loading. However, these methods do not always provide complete sealing to the specimen. In this study, Viton membranes with a special shape (shown in Fig. 3.2) are used to seal both the internal surface of specimen and interface between the specimen and apparatus. High strength epoxy is used to transmit the axial loading.

Figure 3.2 shows the schematic of the apparatus. For multiaxial testing, the SiC/SiC specimen is glued to both the top and bottom steel plates. The specimen and plates are held together using an alignment tool during epoxy curing to avoid eccentricity, shown in Fig. 3.3. A Viton membrane is inserted from the hole of the bottom plate into the SiC/SiC tube while the flange is clamped by bolting the steel bottom plate to the steel pedestal. The O-rings inside the steel pedestal prevent high pressure liquid from leaking through the interface. The specimen and top plate are centered inside the steel clamp and the whole system is bolted to the MTS load frame. The gage length of the specimen is around 40 mm after subtracting the length of adhesive from the specimen length. Based on St. Venant's principle, the central area of the specimen would experience a uniform tensile stress. The present multiaxial testing apparatus is designed for both uniaxial tensile testing and internal pressure testing.

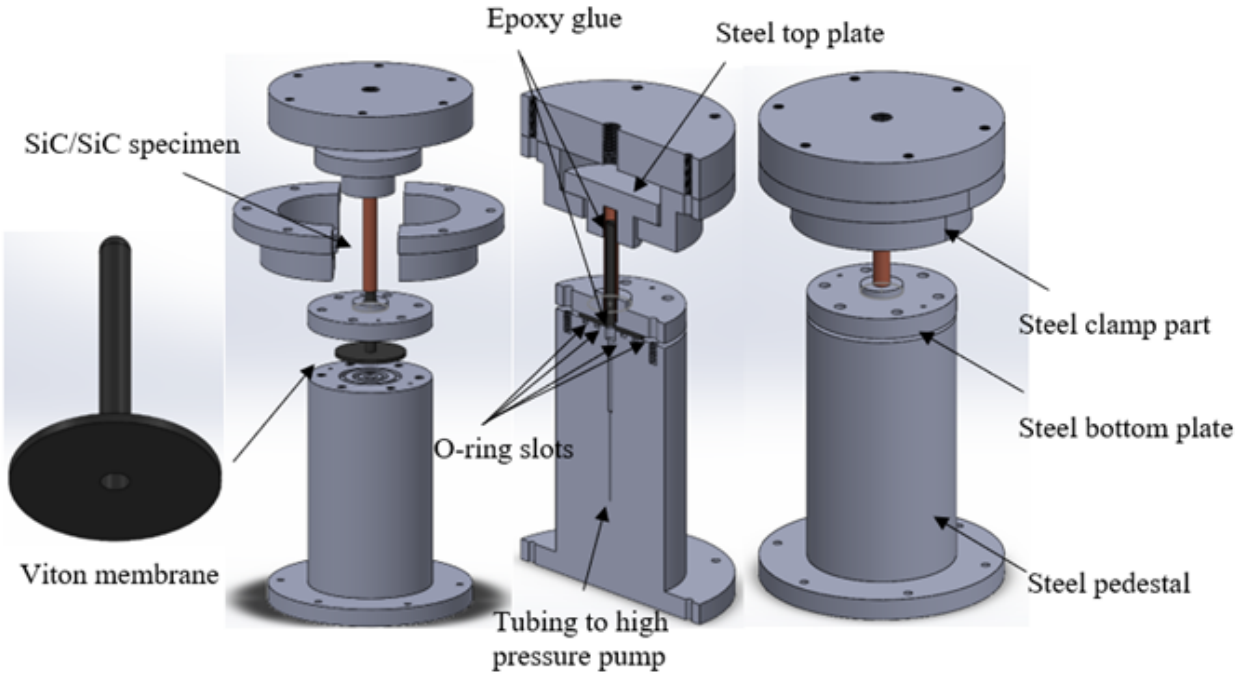

Figure 3.2: Membrane and loading apparatus.

In the experiment, 6-mm long strain gages are attached to the outer surface of the specimen

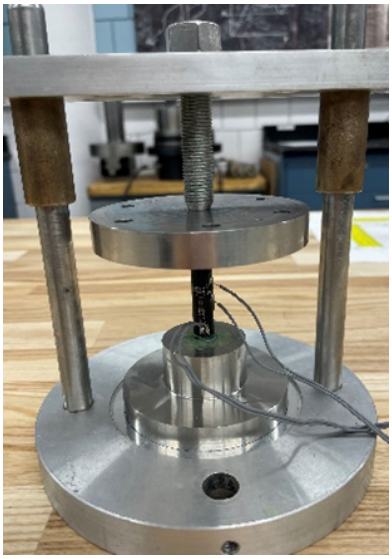

Figure 3.3: Alignment tool.

in both axial and lateral directions. The strain gages can cover several repeating cells of the SiC/SiC composites. The non-flat surface of the woven architecture of SiC/SiC composites makes it difficult to glue strain gages in a single step. The adhesive is first placed on part of the specimen surface and allowed to cure. The hardened epoxy is then lightly sanded and the strain gages are placed on the specimen. In addition to strain measurements, acoustic emission (AE) is used to monitor damage growth. The AE system is composed of (i) AE sensors; (ii) signal filters and preamplifiers; (iii) signal digitizers, and (iv) computer-based data acquisition system. The AE sensors (Physical Acoustics model S9225, frequency response from 0.3-1.8 MHz or Physical Acoustics model Nano-30, frequency response from 0.125–0.75 MHz) are attached to the specimen surface using cyanoacrylate adhesive. The AE signals are pre-amplified with 40 dB gain and band-pass filtered 0.1-1.2 MHz (Physical Acoustic model S1220C). Two four-channel Agilent L4534A digitizers with a sampling rate of 20 MS/s, 16 V full-scale range, and 16-bit resolution are used to record the AE signals continuously. A 4000-sample window provides 0.2 millisecond of recording, with a pre-trigger set at 1500 samples to ensure capturing the first arrival. The digitizers are triggered whenever a selected anchor channel signal reaches the amplitude threshold of 25 mV. To avoid one AE event triggering the system twice, a hold-off time of 10 millisecond between two consecutive events is prescribed. This indicates a maximum AE recording rate of 100 events per second, which is not reached in any of the tests. The time stamps of the trigger are also recorded, which are used for mechanical data analysis.

Figure 3.4 shows the testing and data acquisition system. The closed-loop, servo-hydraulic load frame has multiple control channels, where the axial force, internal pressure, and external pressure can be used as feedback/control signals simultaneously. Data acquisition systems for strains and AE are separated, and therefore synchronization is needed. (For the external pressure test, the pressure vessel would be lowered to create a sealed chamber around the

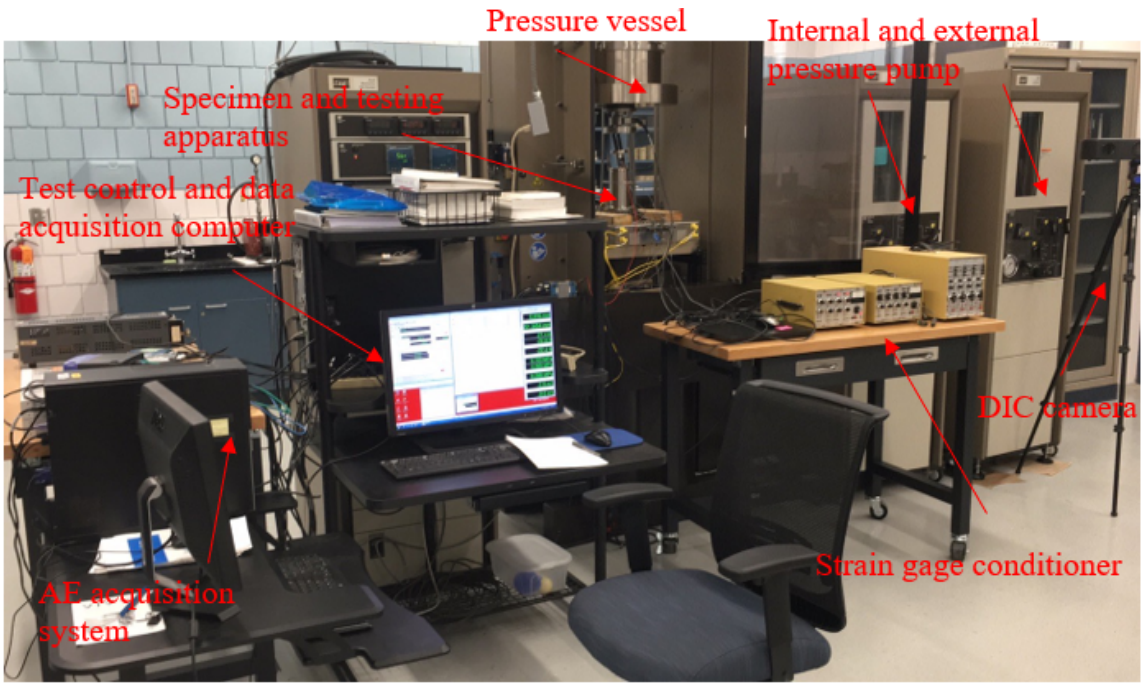

Figure 3.4: Multiaxial testing and data acquisition system.

specimen. The outer surface of the SiC/SiC specimen would be coated with polyurethane to isolate the high-pressure fluid from the specimen.)

3.2 Strain-Based PLS criterion

To investigate the behavior of SiC/SiC specimens under multiaxial stress states, four different load paths are considered in the experiment: uniaxial tension, hoop tension, biaxial tension ($\sigma_{zz}/\sigma_{\theta\theta} = 1$), and one other proportional loading path ($\sigma_{zz}/\sigma_{\theta\theta} = 2$).

For each load path, about 10 successful experiments are performed under the load controlled mode. In order to minimize the effect of loading rate, the same rate is used for all tests. For uniaxial tension and hoop tension tests, loading rates are 2 N/s and 0.03 MPa/s respectively. For multiaxial tests, the major loading rates are fixed to the 2 N/s and 0.03 MPa/s values while the minor loading rates are calculated based on Equations (1) and (2). A typical stress-strain curve from a uniaxial tensile test is shown in Figure 3.5. The UTS or ULS (ultimate limit strength) is recorded as the maximum stress before failure.

ASTM has published recommendations for determining the PLS for uniaxial tension and hoop tension tests (ASTM standards C1275 and C1819). In these recommendations, the PLS is determined as the intersection between the stress-strain curve and a straight line with the slope equal to the Young modulus and an offset of 0.5×10^{-3}. Figure 3.5 shows the PLS determined by this criterion. This approach cannot readily be applied to specimens under multiaxial stress states.

In this study, we propose a new strain criterion in determining PLS for multiaxial stress

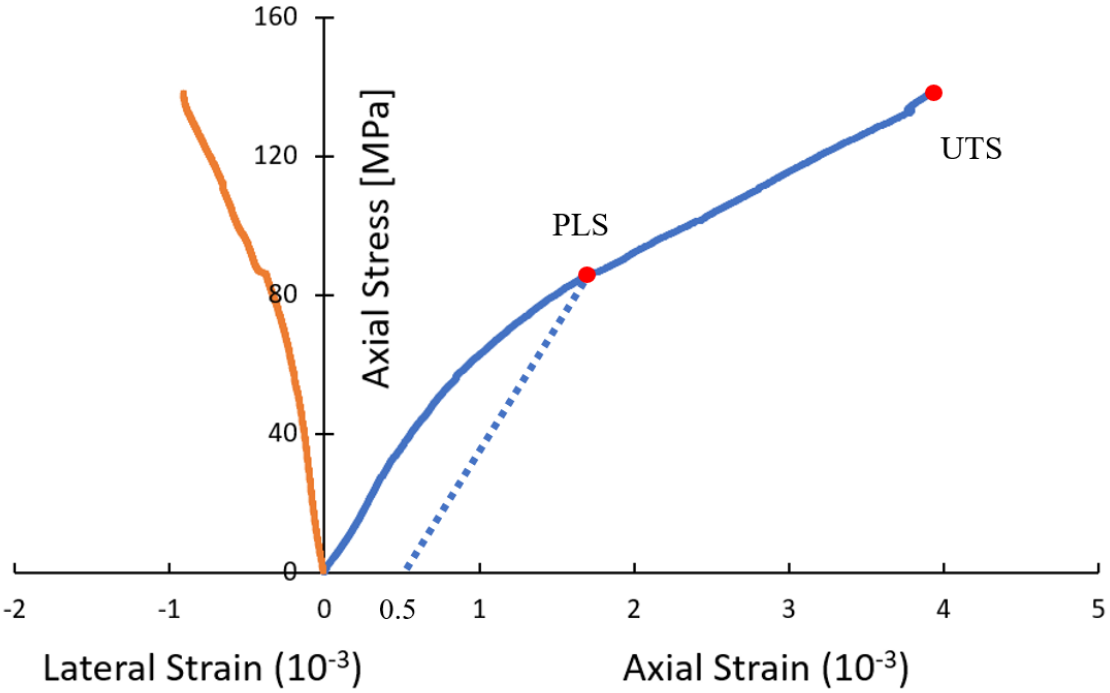

Figure 3.5: Stress-strain response of a uniaxial tension test.

states, which reads

$$\sqrt{\sum_{i,j}(\epsilon_{ij} - \epsilon^e_{ij})^2} = 0.05\% \tag{3.1}$$

where ϵ_{ij} are the measured components of the strain tensor and ϵ^e_{ij} are the theoretical elastic strain components calculated as $\epsilon^e_{ij} = S_{ijkl}\sigma_{kl}$, where S_{ijkl} = elastic compliance. For the uniaxial tension test, when $\sqrt{\sum_{i,j}(\epsilon_{ij} - \epsilon^e_{ij})^2} = 0.05\%$, the lateral strain is very close to that predicted by the elastic solution. Therefore, we have $\sqrt{\sum_{i,j}(\epsilon_{ij} - \epsilon^e_{ij})^2} \approx \epsilon_{zz} - \epsilon^e_{zz} = 0.05\%$, which is essentially the same as the ASTM recommendation.

We further note that Eq. 3.1 is invariant of coordinate system. To show it, denote the present coordinate system by three orthogonal unit vectors $\vec{e}_i$ $(i = 1-3)$, and the new coordinate system by vectors $\vec{e'}_i$. The strain tensor in the new coordinate system can be expressed in terms of the present strain tensor

$$\epsilon'_{ij} = a^m_i a^n_j \epsilon_{mn} \tag{3.2}$$

where $a^q_p = \vec{e'}_p \cdot \vec{e}_q$. To express the strain criterion (Eq. 3.1) in the transformed coordinate system, we first rewrite Eq. 3.1 by

$$\sqrt{\sum_{i,j}(\epsilon'_{ij} - \epsilon'^e_{ij})^2} = \sqrt{\epsilon'_{ij}\epsilon'_{ij} - 2\epsilon'_{ij}\epsilon'^e_{ij} + \epsilon'^e_{ij}\epsilon'^e_{ij}} \tag{3.3}$$

in which we used the Einstein notation. Following Eq. 3.2, we have $\epsilon'_{ij}\epsilon'_{ij} = (\vec{e'}_i \cdot \vec{e}_m)(\vec{e'}_j \cdot \vec{e}_n)(\vec{e'}_i \cdot \vec{e}_p)(\vec{e'}_j \cdot \vec{e}_q)\epsilon_{mn}\epsilon_{pq}$. By noting $\sum_{m=1-3}(\vec{e'}_i \cdot \vec{e}_m)^2 = 1$, it can be shown that $\epsilon'_{ij}\epsilon'_{ij} = \epsilon_{mn}\epsilon_{mn}$.

Likewise, we have $\epsilon'_{ij}\epsilon'^{e}_{ij} = \epsilon_{mn}\epsilon^{e}_{mn}$ and $\epsilon'^{e}_{ij}\epsilon'^{e}_{ij} = \epsilon^{e}_{mn}\epsilon^{e}_{mn}$. Therefore, the strain criterion is invariant with the coordinate system.

3.3 Damage Evaluation via Acoustic Emission

To further investigate the behavior of the SiC/SiC specimens at PLS, we use the cumulative AE count or cumulative AE energy to examine the damage evolution in the specimen. The AE technique is one of the most widely used non-destructive testing techniques for damage evaluation. One major advantage of AE is that the damage processes can be observed during the entire loading history. During the loading process, the formation of new microcracks and subsequent crack propagation generates transient elastic waves. Such waves propagate through the material and are captured by the AE sensors attached to the specimen. Figure 3.5 shows a typical AE waveform (also called an AE event) from a uniaxial tensile test. A sampling time of 100 microseconds (2000 data points) after the first arrival is used to calculate the frequency spectrum with a Fast Fourier Transform (FFT) algorithm and the FFT is shown in Figure 7. It can be seen that the major frequency is between 0.2 and 0.4 MHz.

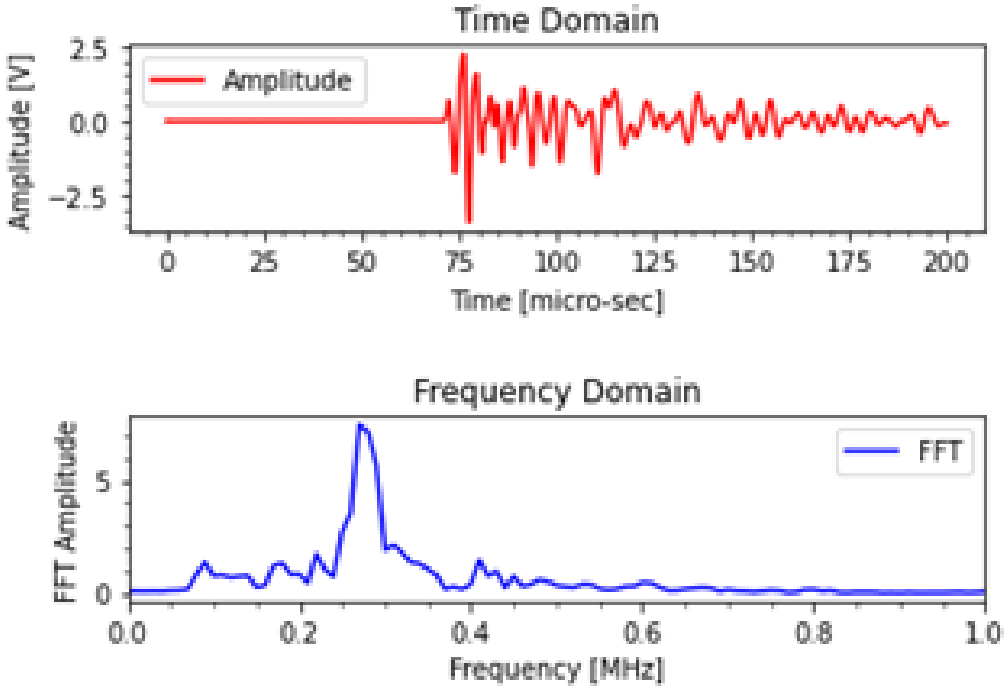

Figure 3.6: A typical AE event and its frequency spectrum.

For each of test on a SiC/SiC specimen, 3000 to 20,000 AE events are typically recorded. These large numbers of AE events could be attributed to the inhomogeneity on a local scale, and the friction between numerous fibers. The AE count rate is calculated as the frequency of AE events recorded. Figure 3.7 shows the AE count rate as well as the corresponding stress state during one of the multiaxial experiments with $\sigma_{\theta\theta} = \sigma_{zz}$. It is observed that AE events

occurred at an early stage of loading and a considerable proportion of the total AE events took place prior to the PLS defined by Eq. 3.1.

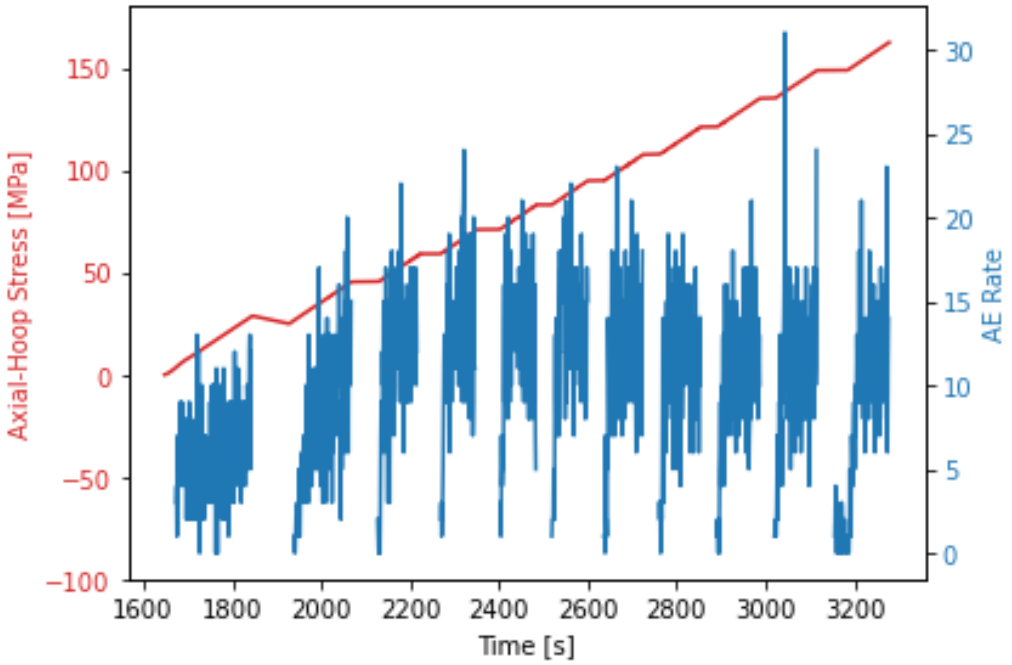

Figure 3.7: AE count rate from a SiC/SiC multiaxial test.

The root-mean-square (RMS) value, which is the square root of the average voltage under the AE waveform, is also used for the analysis of relative energy. The RMS for each AE event is calculated by

$$RMS = \sqrt{\frac{1}{T}\int_{T_0}^{T_0+T} [V(t)]^2 \mathrm{d}t} \tag{3.4}$$

where T_0 is the first arrival time. The time period T should capture the P-wave and the S-wave but not the sensor resonance. Based on the acquired time histories, a time period T of 20 microseconds (i.e. 400 samples from the first arrival point) is used in Eq. 4. After calculating the RMS value for each AE event, the cumulative RMS and cumulative AE count through the entire loading history for one multiaxial test are also determined. The results are shown in Fig 3.8a. The cumulative AE count is shifted by 200 seconds for an easier comparison. From Fig. 3.8a, it is seen that the cumulative plots of RMS and AE count have almost identical shape. Even though the RMS value for each AE event is different, due to the high AE count rate, the summation of the RMS value is proportional to the AE count rate.

Figure 3.8b shows the cumulative AE count and its slope. It can be seen that the rate of cumulative AE counts increases monotonically to its peak and exhibits a mild decrease with strong fluctuation. In some other tests, it is found that the rate of AE counts increases first to the peak followed by fluctuations around the peak value. The initial increase in the rate

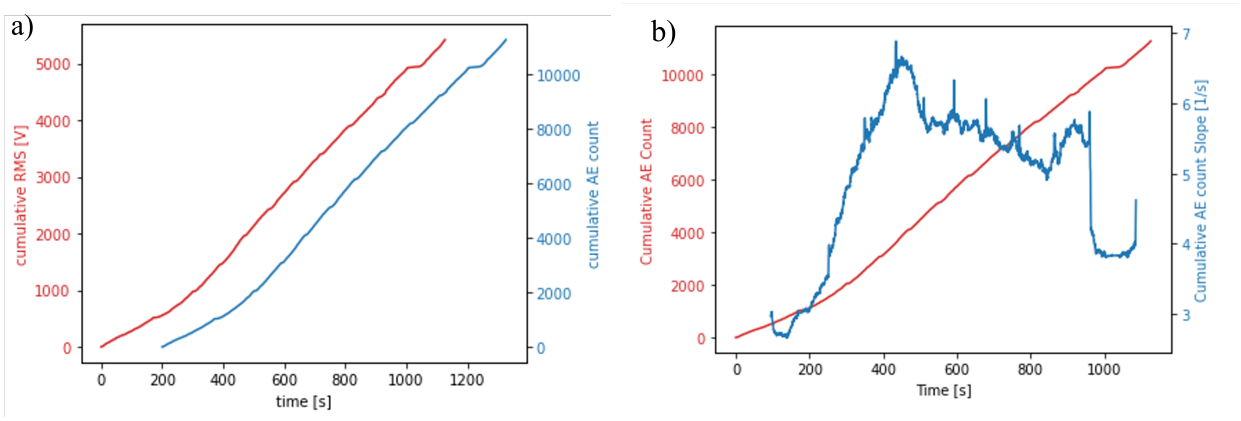

Figure 3.8: (a) Comparison of cumulative RMS and AE count curve, and (b) cumulative AE count curve and its slope from a SiC/SiC multiaxial test.

of AE counts signifies the rapid increase in microcracking in the specimen. As a sufficient number of microcracks form, the microcracks start to nucleate into macrocracks, which leads to a pronounced effect on the stiffness of the specimen. Therefore, it is reasonable to use the peak of the AE count rate to infer the PLS, where we see a clear degradation of the tangential stiffness.

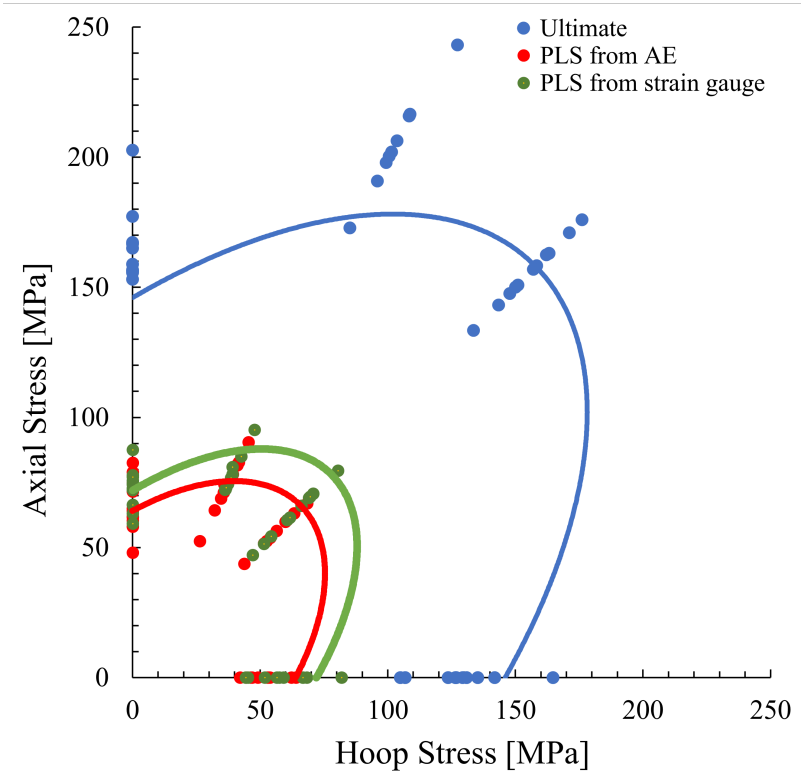

Figure 3.9: Failure surface measured from SiC/SiC multiaxial test.

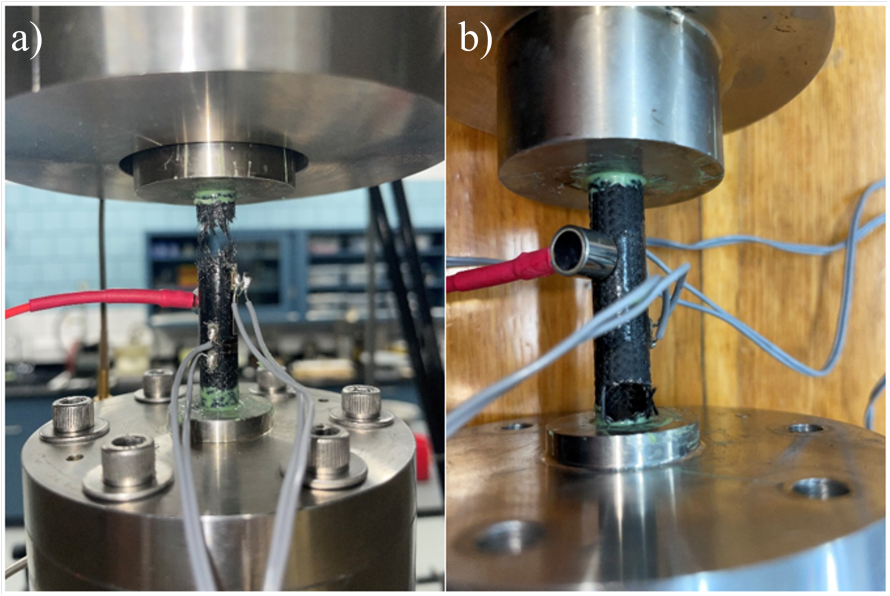

Figure 3.10: Specimen after test under (a) uniaxial tension, and (b) hoop tension.

3.4 Measured PLS Failure Surface

Figure 3.9 shows the surfaces of PLS measured using Eq. 3 and the rate of AE counts, as well as the surface of ULS. All three failure surfaces follow a convex shape. The average value of PLS from AE, PLS from strain gages, and ULS are reported to be 66.51, 71.31 and 165.96 MPa for uniaxial tension tests. These values are larger than those for hoop tension tests, as reported to be 51.49, 59.84 and 129.09 MPa. This clearly shows the anisotropy of SiC/SiC composites. The average biaxial strength of the SiC/SiC specimens are reported to be 55.21, 61.17 and 155.41 MPa for PLS from AE, PLS from strain gage and ULS, while those values for loading of $\sigma_{zz}/\sigma_{\theta\theta} = 2$ are 74.69, 78.40 and 209.87 MPa (hoop stress). It is seen that the PLS determined by Eq. 3.1 is reasonably close to that measured by the rate of AE counts.

Figure 3.10 shows the final failure patterns of the specimens under two loading paths. For specimens loaded by $\sigma_{zz} > \sigma_{\theta\theta}$, the failure is featured by a fracture normal to the cylindrical axis. For specimens loaded with $\sigma_{\theta\theta} > \sigma_{zz}$, catastrophic fracture initiates at the internal surface and propagates through the thickness. Due to the internal pressure control mode, high pressure fluid opens up the crack and the specimen loses its structural integrity, as depicted in Fig. 3.10b.

3.5 Statistics of Multiaxial PLS

One important step for reliability analysis of SiC/SiC claddings is to quantify the variability of the PLS. Motivated by this need, we performed the multiaxial tests on a number of replicates for each loading path. Table 1 lists the results of the PLS of each individual specimen for all four loading paths. Since the present experiments consider proportional loading, we can use a

single parameter η to represent the PLS for each loading path. For axial or hoop tensile test, η is simply equal to the axial or hoop tensile PLS. For biaxial tension $\sigma_{zz} = \sigma_{\theta\theta}$, η is equal to the PLS of σ_{zz} (or $\sigma_{\theta\theta}$). For loading path $\sigma_{zz}/\sigma_{\theta\theta} = 2$, we let η equal to the PLS of σ_{zz} and the corresponding hoop stress is equal to $\eta/2$.

Trial	Uniaxial Tension [MPa]	Hoop Tension [MPa]	Biaxial Tension [MPa]	Multiaxial Tension ($\sigma_z/\sigma_\theta = 2$) [MPa]
1	74.7	53.2	56.4	90.5
2	64.1	62.2	53.8	68.9
3	79	52.8	63.2	82.8
4	48.1	49.1	59.9	52.5
5	58.1	53.8	60.6	64.3
6	82.6	44.5	52.5	81.7
7	60.4	46.3	43.8	71.2
8	61.6	46.9	51.5	78.2
9	65	42.1	-	82.1
10	71.5	64	-	-

Table 1: PLS from Acoustic Emission (parameter η) for all four loading paths

To plot the probability distribution of η, we first rank the values of η of test specimens in the ascending order, and the corresponding cumulative probability is calculated by

$$p_i(\eta) = (i - 0.5)/n \tag{3.5}$$

where i = rank of strength value η, and n = total number of test specimens. Fig. 3.11 shows the measured probability distributions of η plotted on the Weibull scale. Note that, if the data points fall on a straight line, they can be fitted by a two-parameter Weibull distribution. It is seen from Fig. 3.11 that the experimental data cannot be fitted by a straight line. The observed inapplicability of Weibull distribution is well expected for quasibrittle structures since the structure size is not much larger than the zone of damage localization [21, 2]. The application of Weibull strength distribution for quasibrittle structures will be discussed in details in the next chapter.

With the limited amount of test specimens, we can estimate the mean and standard deviation of the PLS for different load paths, which are listed in Table 2. It is seen that the mean value of PLS varies considerably with the load paths. The mean PLS in the axial direction is about 25% lower than that in the hoop direction. On the other hand, the coefficients of variation (CoVs) for different load paths are pretty close. The measured statistics of PLS clearly indicates the anisotropic behavior of the SiC/SiC composites.

We now extend the proposed failure surface (Eq. 2.8) to describe the statistics of PLS. As discussed in Chapter 2, for the present study the failure surface can be fully described by three PLS limits: tensile strength f_{tz} in the axial direction, tensile strength $f_{t\theta}$ in the hoop direction, and biaxial tensile strength f_b. Here we consider these three PLS limits exhibit

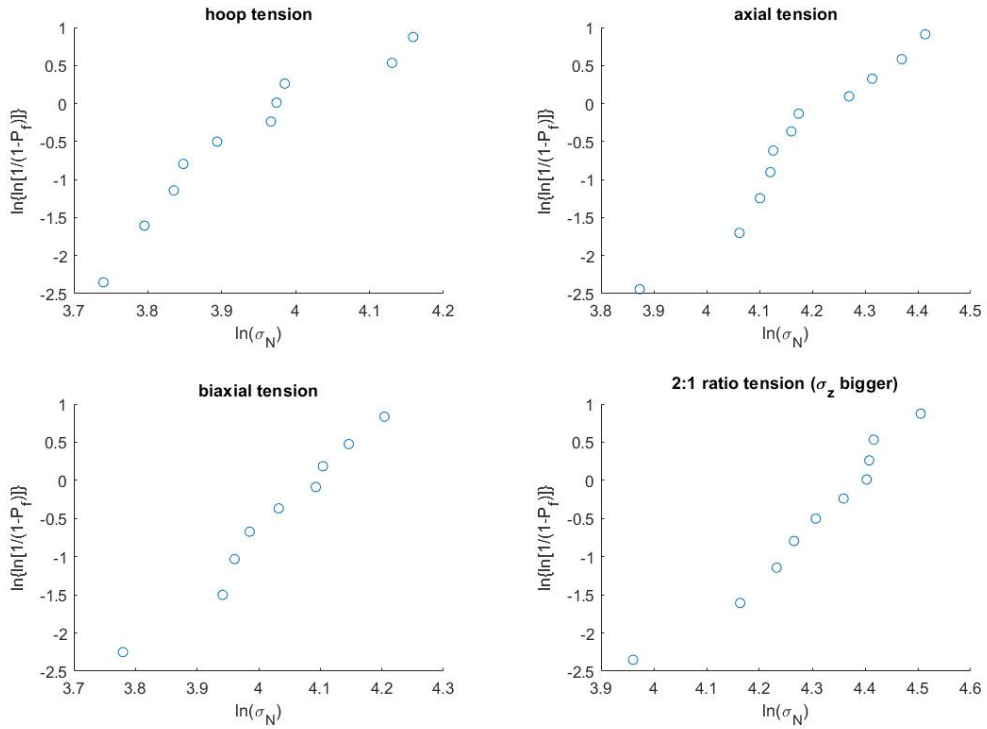

Figure 3.11: Probability distributions of strength in different loading paths.

	Uniaxial Tension [MPa]	Hoop Tension [MPa]	Biaxial Tension [MPa]	Multiaxial Tension ($\sigma_z/\sigma_\theta = 2$) [MPa]
Mean	66.51	51.49	55.21	74.69
Std	9.93	6.87	5.81	10.95
CoVs	0.149	0.133	0.105	0.147

Table 2: Mean, Std and CoVs for all four loading paths

certain randomness, and they follow a Gauss-Weibull probability distribution. This distribution function was recently developed for quasibrittle materials based on atomistic fracture mechanics and a multiscale statistical model [5, 20, 21, 2]. The salient feature of the model is that it captures in the statistical sense both damage localization and load redistribution mechanisms at different scales. The Gauss-Weibull grafted distribution function can be written as

$$F_i(x) = \begin{cases} 1 - e^{(x/s_i)^{m_i}} & (x \leq x_{gi}) \\ P_{gi} + \frac{r_i}{\delta_{Gi}\sqrt{2\pi}} \int_{x_{gi}}^{x} e^{-\frac{(x'-\mu_{Gi})^2}{2\delta_{Gi}^2}} \, \mathrm{d}x' & (x > x_{gi}) \end{cases} \tag{3.6}$$

where subscript $i = tz, t\theta$ and b denote the model parameters for tensile strengths in the axial and hoop directions, and biaxial tensile strength, respectively. m_i and s_i are Weibull modulus and the scale parameter of the Weibull tail; μ_{Gi} and δ_{Gi} are mean and standard deviation of the Gaussian core, if considered extended to $-\infty$; r_i is a scaling parameter required to normalize the grafted cdf such that $F_i(\infty) = 1$; x_{gi} is the grafting point and $P_{gi} = 1 - e^{(x_{gi}/s_i)^{m_i}}$ is the

grafting probability, which is typically on the order of 10^{-3} to 10^{-2} [21, 2]. Since the Weibull tail is very short, the mean and standard deviation of the Gaussian core are almost equal to the mean and standard deviation of the corresponding PLS.

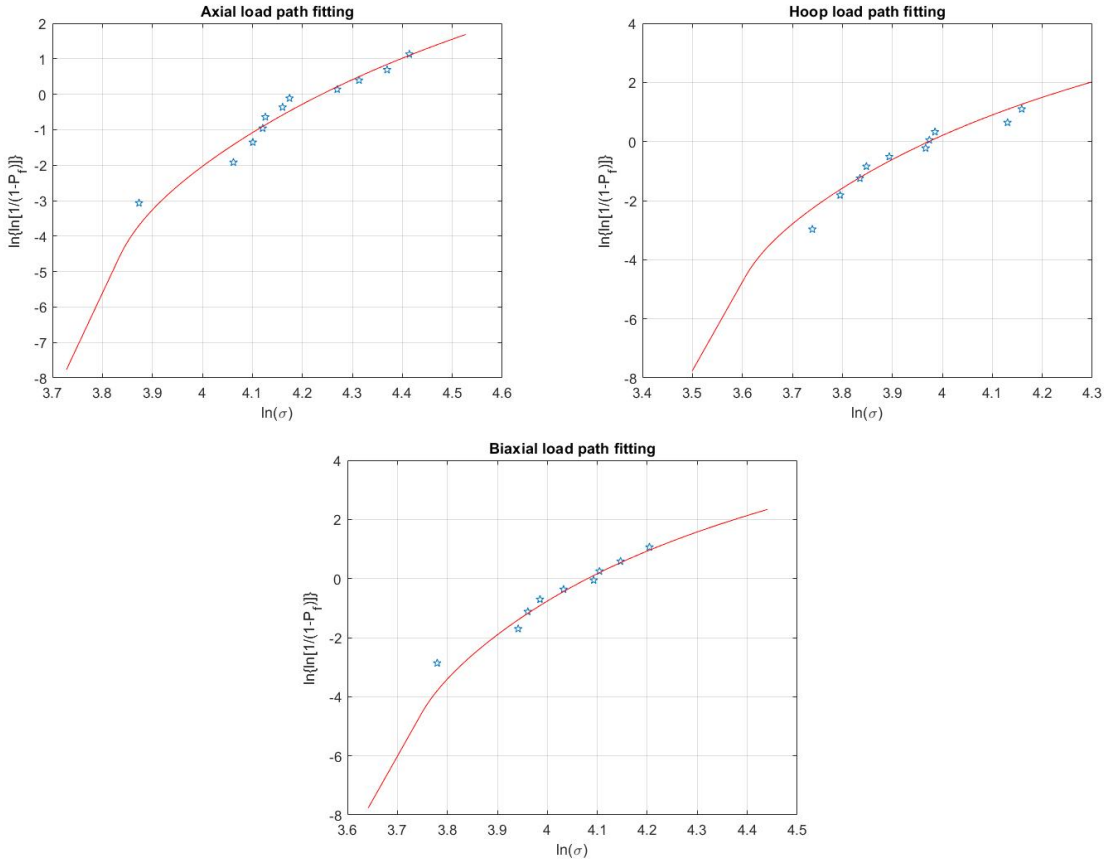

Figure 3.12: Gauss-Weibull fitting of measured histograms of f_{tz}, $f_{t\theta}$ and f_b

	μ_{Gi}	δ_{Gi}	m_i	s_i	x_{gi}	r_i	P_{gi}
$f_{t\theta}$	50.68	7.030	30	42.882	36.779	1.0144	10^{-2}
f_{tz}	65.70	10.232	30	53.891	46.223	1.0190	10^{-2}
f_b	56.75	6.015	30	49.427	42.393	1.0106	10^{-2}

Table 3: Model parameters for fitting histogram of f_{tz}, $f_{t\theta}$ and f_b

In this study, we use Eq. 3.6 to fit the measured histograms of $f_{tz}, f_{t\theta}$ and f_b, as shown in Fig. 3.12. The resulting model parameters are listed in Table 3. Once we determine the probability distributions of $f_{tz}, f_{t\theta}$ and f_b, Eq. 3.6 can be used to predict the failure probability for any loading path. Consider a proportional loading case $\sigma_{zz} = k\sigma_{\theta\theta}$. Based on Eq. 2.8, we have

$$\sigma_{zz} = \left[\frac{k^2}{f_{t\theta}^2} + \frac{1}{f_{tz}^2} - \frac{k}{f_0^2}\right]^{-1/2} \tag{3.7}$$

Based on Eq. 2.7, Eq. 3.7 can be rewritten as

$$\sigma_{zz} = \left[\frac{k^2 - k}{f_{t\theta}^2} + \frac{1-k}{f_{tz}^2} + \frac{k}{f_b^2} \right]^{-1/2} \tag{3.8}$$

With the calibrated probability distributions of f_{tz}, $f_{t\theta}$ and f_b, we can calculate the probability distribution of σ_{zz} by applying the Monte Carlo simulations to Eq. 3.8. We apply this method to the loading case $\sigma_{zz}/\sigma_{\theta\theta} = 2$, and obtain the probability distribution of σ_{zz}. Fig. 3.13 shows the comparison between the measured and predicted probability distributions of PLS for loading path $\sigma_{zz}/\sigma_{\theta\theta} = 2$. It is seen that they match each other reasonably well, which validates the proposed approach.

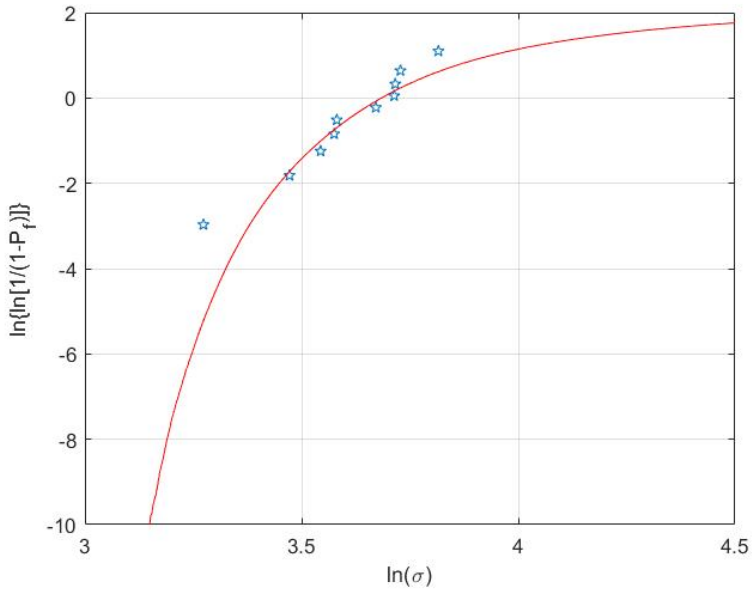

Figure 3.13: Measured and predicted probability distributions of PLS for $\sigma_{zz}/\sigma_{\theta\theta} = 2$

4 Finite Weakest Link Model for Design Extrapolation

The foregoing chapters focused on the failure of laboratory specimens. The laboratory specimens usually have the same cross-sectional dimension as the fuel cladding, but the specimen length is about two orders of magnitude shorter than the fuel cladding. The essential question is how to predict the failure statistics of the full-size cladding from the laboratory test results. To this end, we need to develop a statistical model that is consistent with the failure mechanism. This chapter will present a finite weakest-link model, which physically represents a damage localization mechanism. The model allows efficient calculations of lifetime distribution of the actual cladding. One important consequence is that the lifetime distribution of the cladding would exhibit a strong size(length) effect.

4.1 Background on Weakest-Link Model

The simplest statistical theory for structural strength is Weibull's theory. It is based on the infinite weakest-link model, imagined as an infinite chain (Fig. 4.1), in which each link corresponds to one representative volume element (RVE) of the material. The Weibull theory is based on the following two hypotheses:

1. The structure fails if one RVE fails, as implied by the weakest-link model; and

2. the number of RVEs that could trigger the structural failure is extremely large and can be considered as infinite.

The structural geometry for which the former hypothesis is valid is often called the *positive geometry*. The positive geometry is defined as the structural geometry for which the stress intensity factor (or the energy release rate) at constant load increases as the crack grows. For structures under load control, the failure for such geometry occurs right at the beginning of crack propagation. In the opposite case of negative geometry, the structure does not fail when one RVE softens. Rather, the crack extends under an increasing load in a stable manner, as typically seen in reinforced concrete structures and also achieved in some fracture specimens such as a large panel with a small center crack, loaded on the crack, or in a reverse-taper double-cantilever specimen.

Hypothesis 2 means that, in comparison to structure size D, the FPZ is so small that it can be treated as a point. For geometrically similar structures of various sizes, the stress distribution as a function of relative coordinate vector $\boldsymbol{\xi} = \boldsymbol{x}/D$ of material points is then independent of D ($\boldsymbol{x}$ = actual coordinate vector).

Hypothesis 2 has often gone unmentioned and has usually been considered automatically applicable. But recently it transpired that, for structures made of concrete, fiber composites,

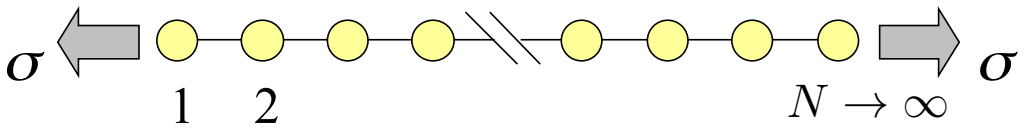

Figure 4.1: Weakest-link model of strength statistics.

---

tough ceramics and other quasibrittle materials, the number of potentially failing RVEs is often far too small to justify the application of Weibull statistics.

Denote P_k = failure probability of the k^{th} RVE ($k = 1, 2, ...N$) of structure, and P_f = failure probability of the structure as a whole. Since positive geometry is assumed, the structure must fail as soon as one RVE fails. In other words, the structure behaves statistically as a chain, which fails as soon as one link fails (Fig. 4.1). The trick to determine P_f is to switch attention from failure probabilities P_k to survival probabilities, which are $1 - P_k$ for each RVE. Obviously, the structure will survive if all its RVEs survive. So, the probability of survival of the structure is the joint probability of survival of all the RVEs. Thus, if we assume that all P_k are statistically uncorrelated (which is acceptable when the autocorrelation length of the random strength field in the structure is not appreciably larger than the spacing of the RVEs), we have, according to the joint probability theorem,

$$1 - P_f = (1 - P_1)(1 - P_2) \cdots (1 - P_N) \tag{4.1}$$

$$\text{or} \quad \ln(1 - P_f) = \sum_{k=1}^{N} \ln(1 - P_k) \approx -\sum_{k=1}^{N} P_k \tag{4.2}$$

Here we introduced the small P_k approximation

$$\ln(1 - P_k) \approx -P_k \tag{4.3}$$

because, in a very long chain, $P_k \ll 1$. The reason is that a very long chain is likely to fail at stress that is in the range of very low probability.

4.2 Weibull theory

Based on his experiments of unprecedented scope (not yet surpassed), Weibull [33, 34] realized that, to fit his test data, the left (low probability) tail of the cumulative distribution function

(cdf) of RVE strength (i.e., failure probability P_k of one RVE) must be a power law[1], i.e.,

$$P_k = [\sigma(\boldsymbol{x}_k)/s_0]^m \qquad \text{for small } \sigma(\boldsymbol{x}_k) \tag{4.4}$$

Here s_0 (of the dimension of stress) and m (dimensionless) are material constants; s_0 is called the scaling parameter, and m the Weibull modulus (or shape parameter); and $\sigma(\boldsymbol{x}_k)$ is the positive part of the maximum principal stress at a point of coordinate vector $\boldsymbol{x}_k$ (we take the positive part because negative normal stresses do not cause tensile fracture). Substituting Eq. 4.4 into Eq. 4.2 and making the limit transition from a discrete sum to an integral over structure volume V (which is justified if the structure consists of many RVEs each of which is much smaller than D), we get the well-known Weibull probability integral;

$$-\ln(1-P_f) \;=\; \sum_k \left(\frac{\sigma(\boldsymbol{x}_k)}{s_0}\right)^m \;\approx\; \int_V \left(\frac{\sigma(\boldsymbol{x})}{s_0}\right)^m \frac{\mathrm{d}V(\boldsymbol{x})}{{l_0}^{n_d}} \tag{4.5}$$

where n_d = number of spatial dimensions in which the structure is scaled ($n_d = 1$, 2 or 3). The integrand

$$c_f(\boldsymbol{x}) = \frac{[\sigma(\boldsymbol{x})/s_0]^m}{{l_0}^{n_d}} \tag{4.6}$$

is called the spatial concentration of failure probability and is the continuum equivalent of P_k of one RVE, whose volume is ${l_0}^{n_d}$. Because the structural strength depends on the minimum strength value in the structure, which is always in the low probability range if the structure is large, the validity of Eq. 4.5 for large enough structures is unlimited.

Eq. 4.5 is contingent upon the assumption that the brittle failure of material occurs in tension (rather than shear or a shear-tension combination), and that the random material strength is the same for each spatial direction, i.e., that the strengths in the three principal stress directions are perfectly correlated. Then it is justified to interpret σ in Eq. 4.5 as the positive part of the maximum principal stress at each continuum point (this stress must be considered as nonlocal when the finite elements are smaller than the RVEs). However, if the random strengths in the principal directions at the same continuum point were statistically independent, then $\sigma^m(x)$ in Eq. 4.5 would have to be replaced by $\sum_{I=1}^{3} \bar{\sigma}_I^m(x)$ where $\bar{\sigma}_I^m(x)$ are the positive parts of the principal nonlocal stresses at that point [11, 4]. Nevertheless, assuming this kind of statistical independence seems unrealistic.

4.3 Scaling of Weibull theory and pure statistical size effect

Consider now geometrically similar structures of different sizes D. In such structures, the dimensionless stress fields $\bar{\sigma}(\boldsymbol{\xi})$ are the same functions of dimensionless coordinate vector $\boldsymbol{\xi} =$

[1] In 1928, Fisher and Tippet [10], working at Cambridge University, evidently unknown to Weibull, came to the same conclusion by mathematical arguments based on the stability postulate of extreme value statistics (as explained later in this chapter).

$\boldsymbol{x}/D$, i.e., they depend only on structure geometry but not on structure size D. In Eq. 4.5, we may then substitute

$$\sigma(\boldsymbol{x}) = \sigma_N \bar{\sigma}(\boldsymbol{\xi}) \quad (\boldsymbol{\xi} = \boldsymbol{x}/D) \tag{4.7}$$

where σ_N = nominal stress = P/bD where P is the applied load or a conveniently defined load parameter, and b = structure width (which may but need not be scaled with D). Further we may set

$$\mathrm{d}V(\boldsymbol{x}) = D^{n_d}\mathrm{d}V(\boldsymbol{\xi}) \tag{4.8}$$

After rearrangements, Eq. 4.5 yields $-\ln(1-P_f) = (\sigma_N/S_0)^m$ or

$$P_f \;=\; 1 - \mathrm{e}^{-(\sigma_N/s_0)^m \Psi (D/l_0)^{n_d}} \;=\; 1 \;-\; \mathrm{e}^{-(\sigma_N/S_0)^m} \tag{4.9}$$

where
$$S_0 = s_0 (l_0/D)^{n_d/m} \Psi^{-1/m}, \quad \Psi \;=\; \int_V [\bar{\sigma}(\boldsymbol{\xi})]^m \;\mathrm{d}V(\boldsymbol{\xi}) \tag{4.10}$$

According to Eq. 4.9, the tail probability of structural failure is a power law:

$$P_f \;\approx\; (\sigma_N/S_0)^m \qquad (\text{for } \;\sigma_N \to 0) \tag{4.11}$$

For $P_f \leq 0.02$ [or 0.2], its deviation from Eq. 4.9 is $< 1\%$ [or < 10 %] of P_f.

The effect of structure geometry is embedded in integral Ψ, which is independent of the structure size. Because exponent m in this integral is typically > 20 (and $0.8^{20} = 0.012$), the regions of structure in which the stress is less than about 80% of material strength have a negligible effect.

Note that P_f depends only on the parameter

$$s_0^* = s_0 {l_0}^{n_d/m} \tag{4.12}$$

and not on s_0 and l_0 separately. So, the material characteristic length l_0 is used here only for convenience, to serve as a chosen unit of measurement. The Weibull statistical theory of strength, per se, has no characteristic length (which is manifested by the fact that the scaling law for the mean strength is a power law [1]).

The last expression in Eq. 4.9 is the Weibull distribution in standard form, with scale parameter S_0. From Eq. 4.10 one finds that

$$\sigma_N \;=\; C_0 \;(l_0/D)^{n_d/m} \tag{4.13}$$

where
$$C_0 = C_f \Psi^{-1/m}, \quad C_f = s_0[-\ln(1-P_f)]^{1/m} \tag{4.14}$$

This equation, in which C_0 and S_0 are independent of D, describes the scaling of nominal strength of structure when the failure probability P_f is specified.

The mean nominal strength is calculated as (Fig. 4.2):

$$\bar{\sigma}_N = \int_0^\infty \sigma_N p_f(\sigma_N)\mathrm{d}\sigma_N = \int_0^1 \sigma_N \mathrm{d}P_f = \int_0^\infty (1-P_f)\mathrm{d}\sigma_N \tag{4.15}$$

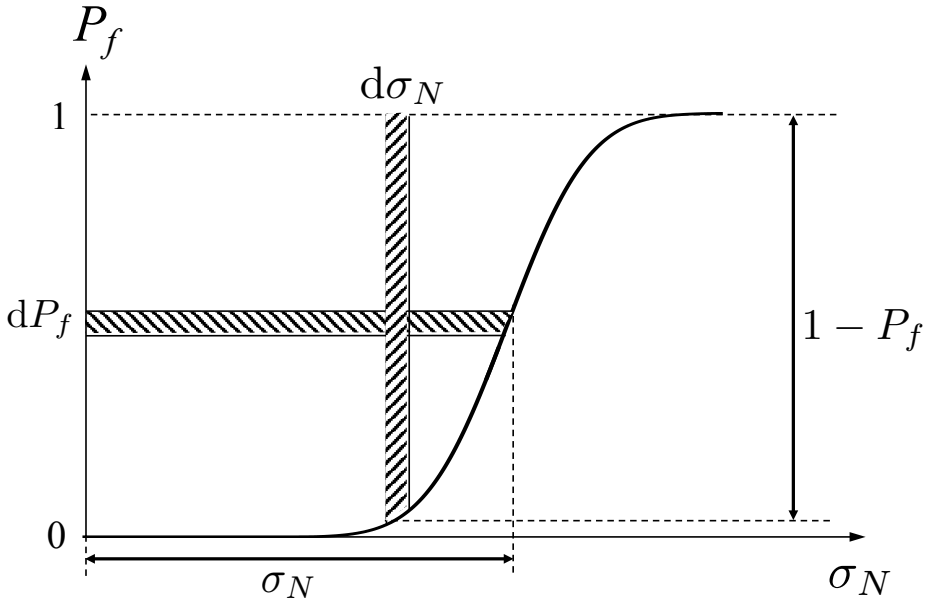

Figure 4.2: Calculation of mean structural strength.

---

where $p_f(\sigma_N) = \mathrm{d}P_f(\sigma_N)/\mathrm{d}\sigma_N$ = probability density function (pdf) of structural strength, while $P_f(\sigma_N)$ = strength cdf. Substituting Eq. 4.9 and noting that $\int_0^\infty t^{z-1}e^{-t}\mathrm{d}t = \Gamma(z) =$ gamma function, one gets, after rearrangements, the well-known Weibull scaling law for the mean nominal strength as a function of structure size D and geometry parameter Ψ;

$$\bar{\sigma}_N(D,\Psi) \;=\; s_0\Gamma(1+1/m) \;=\; C_s(\Psi)\; D^{-n_d/m} \tag{4.16}$$

where
$$C_s(\Psi) \;=\; \Gamma(1+1/m)\; {l_0}^{n_d/m} s_0/\Psi^{1/m} \tag{4.17}$$

For the gamma function one may use the approximation $\Gamma(1+1/m) \approx 0.6366^{1/m}$, which is accurate within the range $5 \le m \le 50$ (Eq. 12.1.22 in [4]).

The coefficient of variation (CoV) of σ_N is calculated as

$${\omega_N}^2 = {\bar{\sigma}_N}^{-2} \int_0^\infty (\sigma_N - \bar{\sigma}_N)^2 p_f \mathrm{d}\sigma_N = {\bar{\sigma}_N}^{-2} \int_0^\infty {\sigma_N}^2 \; \mathrm{d}P_f(\sigma_N) - 1 \tag{4.18}$$

where $\mathrm{d}P_f(\sigma_N)/\mathrm{d}\sigma_N = p_f(\sigma_N) =$ pdf of σ_N. Substitution of Eq. 4.9 gives, after rearrangements, the following well-known expression for the strength CoV:

$$\omega_N = \sqrt{\frac{\Gamma\,(1+2/m)}{\Gamma^2\,(1+1/m)} - 1} \tag{4.19}$$

which is independent of structure size as well as geometry. Approximately, $\omega_N \approx (0.462 + 0.783m)^{-1}$ for $5 \le m \le 50$ (Eq. 12.1.28 in [4]).

4.4 Finite Weakest-Link Model for SiC/SiC cladding

The previous sections discussed the infinite weakest-link model for structural strength and the consequent Weibull strength distribution. One important implication of the Weibull strength distribution is the size dependence of strength statistics, often referred to as the Weibull size effect. However, the infinite weakest-link model represents a limiting case, in which the smallest element triggering the failure of the entire structures is far smaller than the overall structure size. This condition is not often met in many practical cases. Therefore, the measured probability distribution of structural strength does not follow the Weibull distribution. In this study, we consider the cladding fails as soon as damage initiates from anywhere. Therefore, the cladding survives if and only if all the material elements survive. Mathematically, the failure statistics of the cladding can be represented by a weakest-link model.

First consider a laboratory specimen. At failure damage would localize into one material element. The size of this material element is related to the width of the fracture process zone. For SiC/SiC composites, the size of the material element which damage localizes is expected to be on the order of the tow width ($\approx$ 1.2 mm). By assuming that the failure statistics of each material element is statistically independent, the failure probability $P_{fs}(t)$ of the specimen subjected to a general loading history can be calculated by

$$P_{fs}(t) = \Pr(t_f \leq t) = 1 - [1 - P_1(t)]^{n_s} \tag{4.20}$$

where $P_1(t)$ = failure probability of one material element, and n_s = number of material elements in the specimen. Eq. 4.20 is written by assuming that the all the material elements experience the same stress history up to failure. It is noted that in laboratory testing we normally cannot directly obtain the strength distribution P_1 of one material element. Instead, we can measure the failure probability of a specimen, from which we infer $P_1(t)$ as

$$P_1(t) = 1 - [1 - P_{fs}(t)]^{1/n_s} \tag{4.21}$$

Now consider an actual SiC/SiC cladding. Recent studies have shown that during its service lifetime the cladding experiences a non-uniform stress distribution [28]. To account for the non-uniformity of the stress field, we can write the finite weakest-link model as

$$P_f(t) = 1 - \prod_{j=1}^{n} [1 - P_1(\boldsymbol{\sigma}_j, t)] \tag{4.22}$$

where n = number of material elements in the cladding, and $\boldsymbol{\sigma}_j$ = a vector containing the stress components σ_i for jth material element. Eq. 4.22 can be conveniently rewritten by taking the logarithmic, which will allow us to replace the product by a summation, i.e.

$$\ln [1 - P_f(t)] = \sum_{j=1}^{n} \ln [1 - P_1(\boldsymbol{\sigma}_j, t)] \tag{4.23}$$

Since there are many elements in the cladding, we can replace the summation by integration. Eq. 4.23 can be rewritten as

$$P_f(t) = 1 - \exp\left\{\frac{1}{V_0}\int_V \ln\left\{1 - P_1[\boldsymbol{\sigma}(x,t),t]\right\} \mathrm{d}V\right\} \tag{4.24}$$

where V_0 = volume of one material element. By substituting Eq. 4.21 into Eq. 4.24, we have

$$P_f(t) = 1 - \exp\left\{\frac{1}{V_s}\int_V \ln\left\{1 - P_{fs}[\boldsymbol{\sigma}(x,t),t]\right\} \mathrm{d}V\right\} \tag{4.25}$$

where V_s = volume of laboratory test specimen. $P_{fs}[\boldsymbol{\sigma}(x,t),t]$ represents the failure probability of the test specimen at time t when subjected to stress history $\boldsymbol{\sigma}(t)$ that is experienced by a material point located at x of the actual cladding. As mentioned in Chapter 2, $P_{fs}[\boldsymbol{\sigma}(x,t),t]$ can be calculated through Monte Carlo simulations based on the known cdf's of f_{tz}, $f_{t\theta}$ and f_b through Eq. 2.15.

Eq. 4.25 provides a closed-form relationship between the failure statistics of test specimen and the full-size cladding. The model has two important features:

- The model captures the effect of cladding length on the failure probability of the cladding. It is well expected that, similar to the infinite weakest-link model, Eq. 4.25 would predict a strong length effect on the failure probability of the cladding. Understanding this size effect is essential for design extrapolation across claddings of different lengths.

- The model takes into account the effect of the time-varying load history. It is noted that the use of $P_{fs}[\boldsymbol{\sigma}(x,t),t]$ indicates that the failure probability at any given time depends on not only the current stress state, but also the previous load history. This dependence arises from the damage kinetics model, which naturally captures the effect of load path on the damage accumulation.

5 Reliability Analysis of SiC/SiC Claddings

The present model is applied to evaluate the reliability of SiC/SiC claddings. The purposes of this analysis are 1) to demonstrate the application of the model for reliability analysis of full-length claddings, 2) to investigate the effect of cladding length on the failure probability, and 3) to understand the effect of subcritical damage growth on the failure probability.

5.1 Description of Analysis

The stress history used in the analysis was extracted from a recent thermo-mechanical analysis of SiC/SiC cladding [28]. The analysis is concerned with a 4m long SiC/SiC composite cladding under a service lifetime of 2 years. The cladding is subjected to a combination of external pressure, internal pressure, temperature, and irradiation induced swelling. The external pressure is kept at 15 MPa over the entire period of time whereas the internal pressure increases linearly from 1 MPa to 20 MPa. The thermal loading is applied to both the internal and external surfaces. The linear heating rate varies along the cladding height. The details of the thermal loading and boundary conditions can be found in [28]. The irradiation dose increases linearly from 0 to 6 dpa over the 2 year period. In the analysis, the constitutive behavior of the SiC/SiC material is described by an anisotropic constitutive model, in which the elastic stiffnesses degrade with the irradiation induced swelling. In addition, the constitutive model also takes into account the temperature-dependent thermal expansion and conduction.

The numerical analysis showed that the cladding experiences compressive stresses in both axial and hoop directions at the beginning due to the external pressure. During this early loading stage, the compressive axial and hoop stresses at the inner region of the cladding are higher than those at the outer region since the inner surface is subjected to a higher temperature than the outer surface. As the loading proceeds, the cladding experiences irradiation induced swelling. The amount of swelling is strongly dependent on the temperature. The non-uniform spatial distribution of temperature leads to a spatial variation of swelling in the cladding, which drives the evolution of the internal stress distribution. The simulation showed that, over the service lifetime, the hoop stress at the inner surface changes from 152 MPa in compression to 73 MPa in tension and the axial stress rises from 88 MPa in compression to 51 MPa in tension. The change of stresses at the outer surface is less significant. Fig. 5.1 shows the time evolution of the axial and hoop stresses at the inner layer of the cladding at its mid-height. It is seen that the hoop stress increases at a rate much larger than the axial stress does, as predicted by the elastic solution of the hoop and axial stresses of thin-wall structures.

Over the majority of the loading duration, the inner region of the cladding experiences axial tension, and the hoop stress also turns to be tensile after 12 months. By contrast, the outer region is primarily under mild compressive stresses as compared to the material compressive

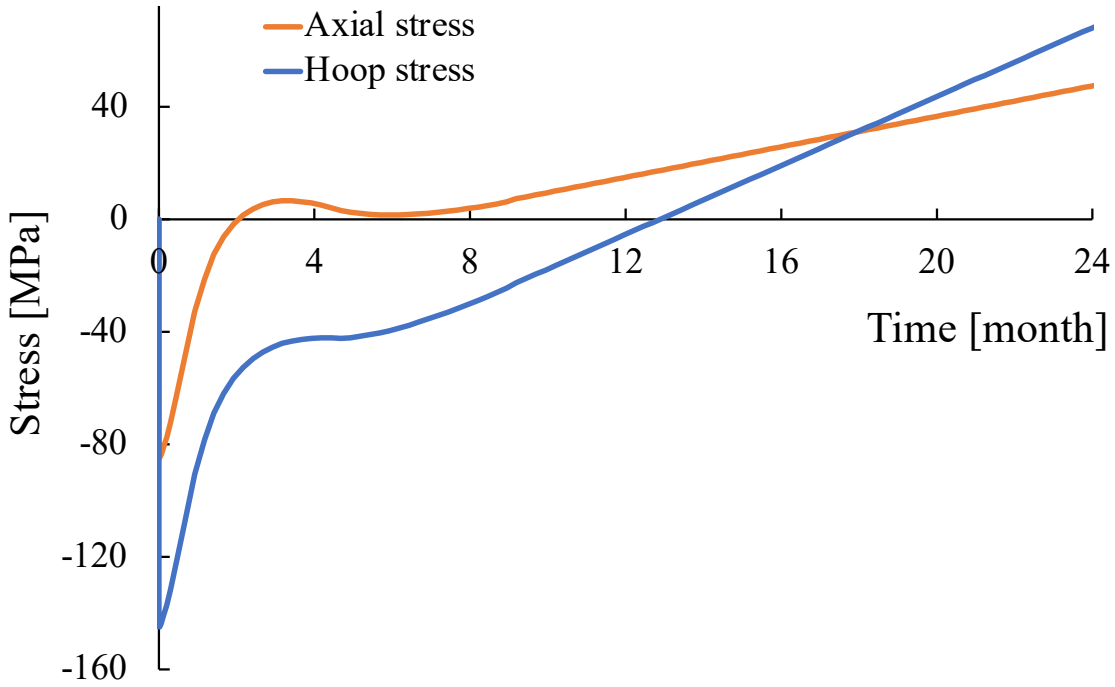

Figure 5.1: Time histories of axial and hoop stresses of the inner layer of the cladding at its mid-height [28].

strength. Fig. 5.2 shows the variation of axial and hoop stresses at the inner surface along the height of the cladding at the end of loading. It is seen that the cladding experiences a uniform stress along its height except towards the two ends. The drastic change of axial stress at the two ends is attributed to the lower temperature, which affects the the irradiation induced swelling.

Based on the stress history of the cladding simulated in this recent study [28], we calculate the in-plane principal stresses, which are input to the present probabilistic model. As discussed in Sec. 3.5, the probability distributions of PLS limits f_{tz}, $f_{t\theta}$, and f_b are considered to follow a Gaussian-Weibull grafted distribution, and the statistical parameters are determined by the multiaxial tests. By knowing these distribution functions, we can calculate the failure probability of the cladding at any given time during the loading process. Since the stress histories are calculated by a finite element analysis [7], it is natural to rewrite Eq. 4.25 by

$$P_f(t) = 1 - \exp\left\{\frac{1}{V_s}\sum_j \ln\left\{1 - P_{fs}[\boldsymbol{\sigma}_j(x,t),t]\right\}\Delta V_j\right\} \tag{5.1}$$

where $\boldsymbol{\sigma}_j$ = stress tenor of finite element j and ΔV_j = volume of finite element j. Based on Eq. 2.15, it is not possible to obtain a closed-form solution for $P_{fs}[\boldsymbol{\sigma}_j(x,t),t]$. Therefore, we rely on Monte Carlo simulations to evaluate the failure probability P_{fs} of each finite element. For any given finite element, we first sample the uniaxial tensile and compressive strengths and biaxial tensile strength by

$$f_i = F_i^{-1}(u_i) \quad (i = tz, t\theta, b) \tag{5.2}$$

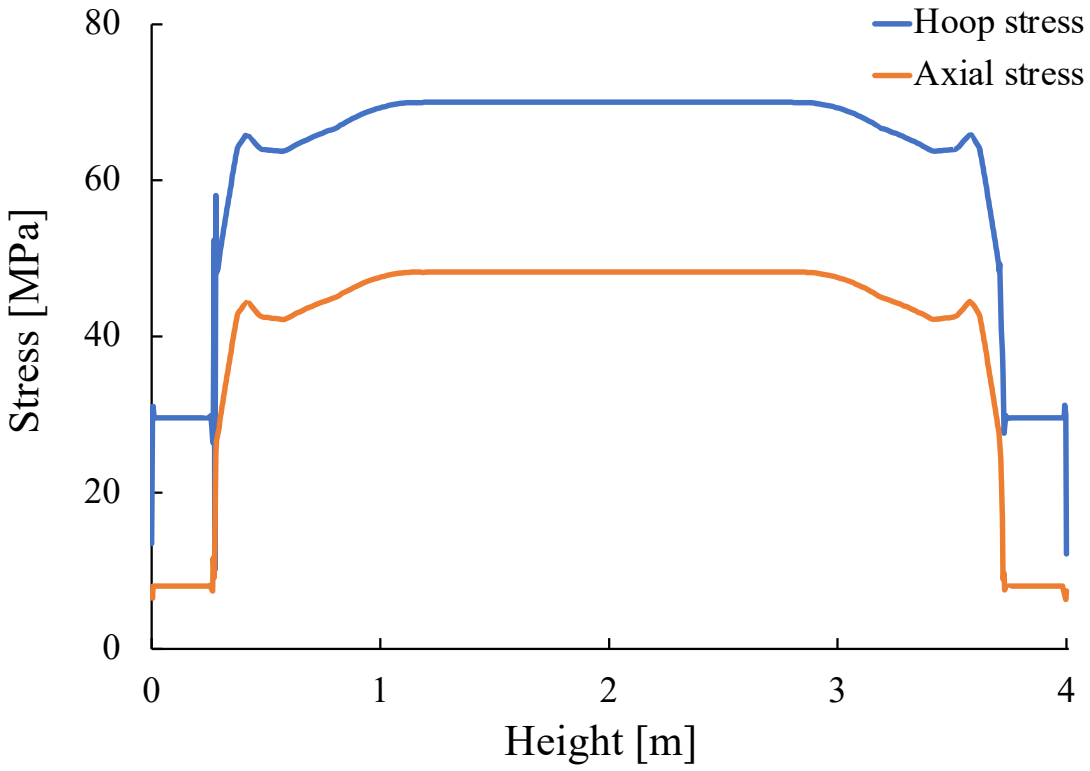

Figure 5.2: Spatial distribution of axial and hoop stresses at 2 year of service along the height of the cladding [28].

where u_i = sampled value of a random variable u that is uniformly distributed over the range of 0 to 1. For a given set of $f_{tz}, f_{t\theta}, f_b$ and the stress history, the time-to-failure t_f of each element can be determined from Eq. 2.15. By repeating this calculation for a large number of realizations of $f_{tz}, f_{t\theta}, f_b$, we can calculate the failure probability P_{fs}. The simulated failure probabilities of finite elements are then input to Eq. 5.1 for determining the failure probability of the entire cladding.

5.2 Time Evolution of Failure Probability

In the recent FE analysis, the cross section of the cladding is discretized into 6 layers in the radial direction. The thermomechanical loading and irradiation cause a strong non-uniform stress distribution across these layers. In this section, we first analyze the time evolution of the failure probability of the inner layer of the cladding. The simulation results showed that a large part of the inner layer experiences a uniform stress distribution except for the end regions [28]. Here we consider a uniform stress distribution for the inner layer along the cladding height. For the later analysis of the failure risk of the cladding, the actual stress profile will be used.

Fig. 5.3 shows the calculated failure probability of the inner layer. It is seen that the failure probability increases monotonically over time. As mentioned earlier, the failure probability $P_f(t)$ is defined by $P_f(t) = \Pr(t_f \leq t)$. Physically it represents the failure probability of the

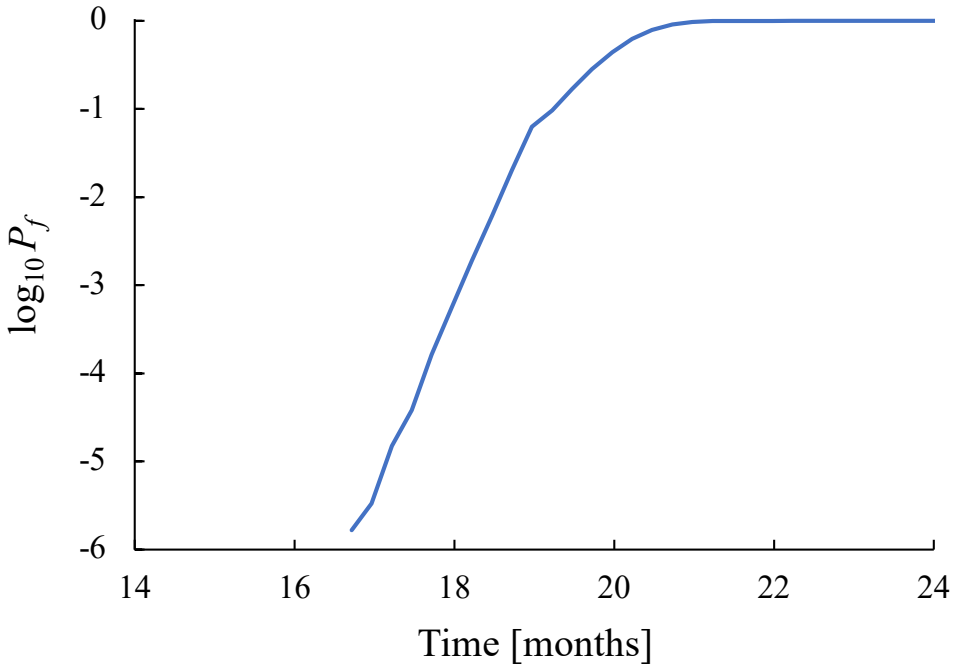

Figure 5.3: Failure probability of the inner layer of the cladding calculated using the stresses at its mid-height.

structure taking into account the entire loading history up to time t. For a given loading history, $P_f(t)$ is a monotonic non-decreasing function. In the present study, the accumulative effect of the past loading history on the failure probability is captured by the damage accumulation model. The failure probability of the structure during a time period $\delta t = t_2 - t_1$ can then be calculated by $P_f(\delta t) = P_f(t_2) - P_f(t_1)$.

Fig. 5.4 presents the time evolution of the contribution of the applied stress on the damage growth by using the mean values of f_t and f_c. As indicated by Fig. 5.1, during the first 8 months, the material experiences compressive stresses in both axial and hoop directions. However, the absolute difference in the in-plane principal stresses is very small as compared to the compressive strength. Therefore, the risk of compression-induced shear failure is negligibly small and the damage growth rate is very low. After 13 months, both axial and hoop stresses become tensile leading to the acceleration of the damage growth. However, the difference between the hoop and axial stresses decreases, which leads to a decrease in the failure risk. After 18 months, the tensile axial and hoop stresses continue to grow, and meanwhile the difference between these stress components starts to increase. This causes a considerable increase in the damage growth rate.

The foregoing analysis of the time history of damage growth is directly reflected by the time evolution of failure probability. It is seen that failure probability is relatively small ($< 10^{-5}$) for the first 17 months. Over the last 6 months, the failure probability increases quickly to 1. This is due to the fact that during that period both the axial and hoop stresses increase to a

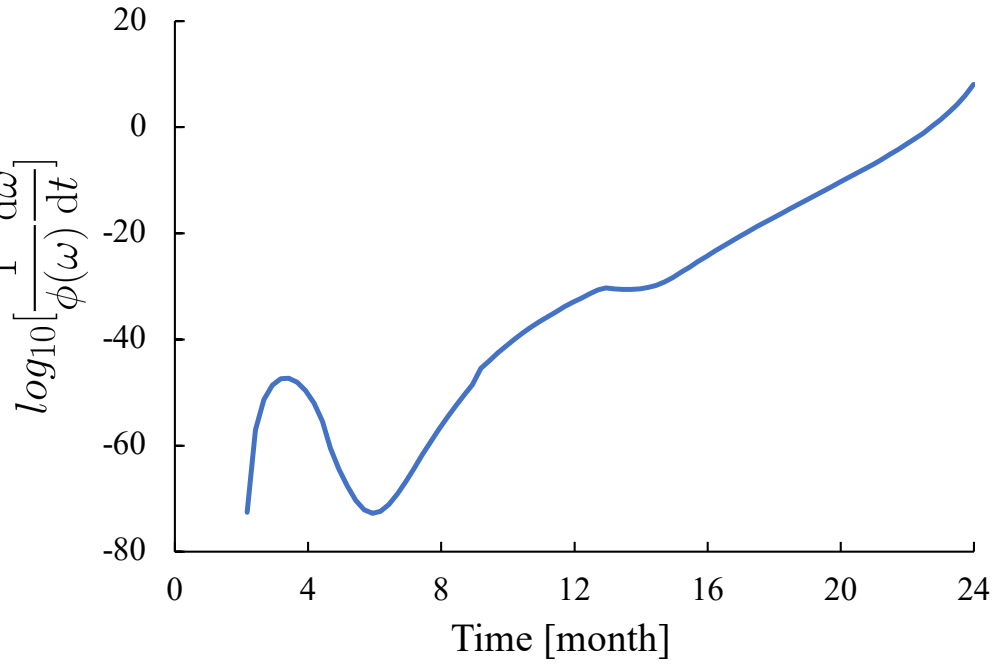

Figure 5.4: Time evolution of contribution of applied stress on the damage growth at the mid-height of the inner layer.

considerable level as compared to the tensile strength of the material.

5.3 Spatial Distribution of Failure Probability

It is also of practical interest to investigate the spatial distribution of failure probability. This information not only reveals the most vulnerable part of the structure, but also has profound implications for the scale effect on the failure probability. Based on the stress histories calculated from the finite element analysis [28], we determine the spatial distribution of failure probability P_f of one column of finite elements of the inner layer at the 24th month of service, as shown in Fig. 5.5.

It is seen that the failure probability of material elements is nearly a constant over the entire cladding except for the two end regions. This is consistent with the spatial distribution of the stress profile as shown in Fig. 5.2. This indicates that the damage has an equal likelihood to occur at any location over the 3m length of the cladding. The uncertainty of the potential damage location indicates a strong weakest link effect on the overall failure statistics. The direct consequence is that the failure probability of the layer would increase with the length of the cladding. Moreover, the type of failure probability function could vary with the cladding length [2]. This size effect must be taken into account in reliability-based design of the cladding. By contrast, if the layer experiences a strongly non-uniform stress distribution, then the failure location could be deterministic. In this case, the failure probability of the layer is

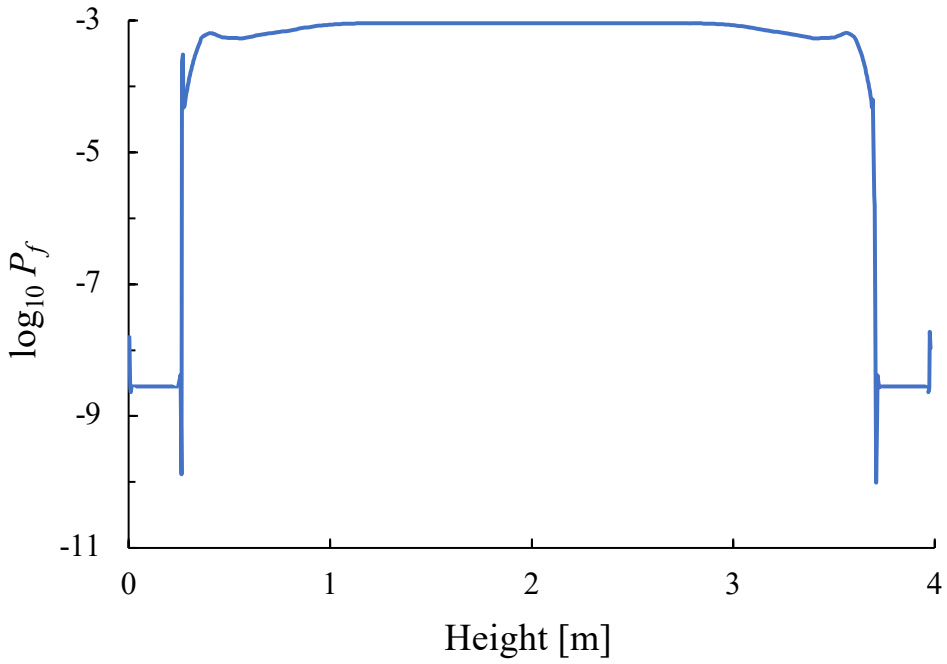

Figure 5.5: Spatial distribution of failure probability of one column of inner-layer elements over a period of 24 months.

determined solely by the particular material element at the failure location, and therefore the failure statistics is independent of the cladding length.

5.4 Failure Probability of Entire Cladding and the Effect of Damage Growth Rate

Fig. 5.6 presents the evolution of the failure probability of the entire cladding over the its service period calculated based on the stress histories reported in [28]. It is seen that the failure probability of the cladding grows monotonically over time up to 5.2%. The FE stress analysis showed that the outer layer of the cladding primarily experiences compressive stresses in both hoop and axial directions over the entire loading period, whereas the hoop and axial stresses of the inner layer change from compression to tension as loading proceeds [28].

During the first 18 months of service, the entire cladding experiences compressive stresses. Based on the failure criterion, this could lead to compression-induced shear. In this case, the entire cross section of the cladding contributes to the failure probability. This explains why the failure probability of the cladding is higher than that of the inner layer for the first 18 months. Nevertheless, it should be pointed out that the inner layer experiences higher compressive stresses as compared to the outer layer, and therefore the inner layer is more vulnerable than the outer layer during the early stage of the loading process. After 18 months, the inner layer of the cladding starts to experience tension. Since the compressive strength is considerably higher than the tensile strength, the tensile stresses experienced by the inner layer give rise to

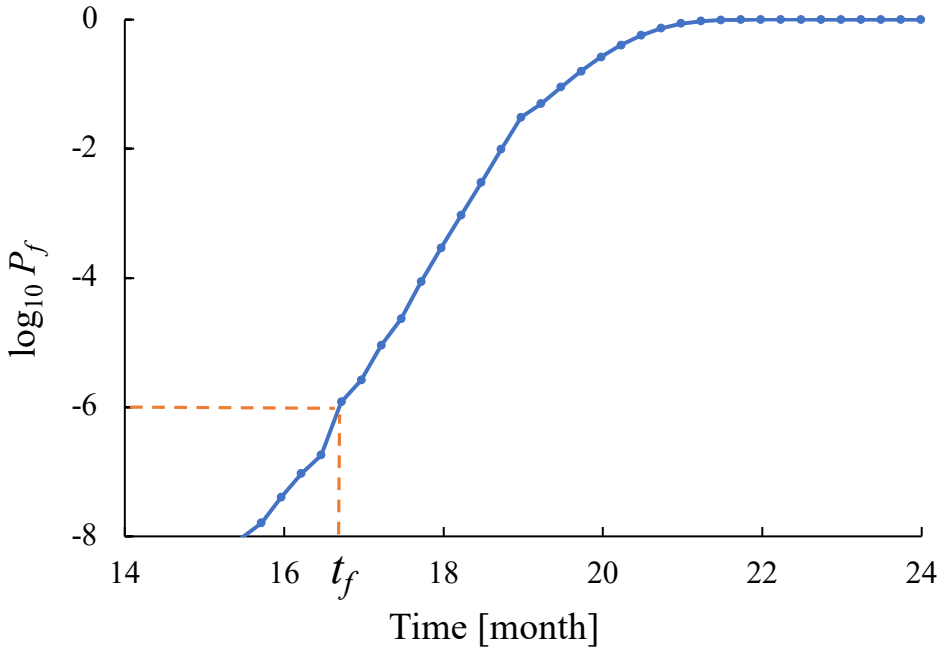

Figure 5.6: Lifetime distribution of the entire cladding; for a tolerable failure risk of 10^{-6}, the cladding should be inspected after $t_f = 16.6$ months of service.

a significant level of failure probability. By contrast, the risk of failure due to the compression-induced shear is very low. Consequently, the overall failure probability of the cladding at the end of its service is primarily governed by the inner layer.

Fig. 5.6 provides critical information on when the inspection and maintenance are needed to guard against a given tolerable failure risk. Based on Fig. 5.6, for a tolerable failure risk of 10^{-6}, the cladding should be inspected after 16.6 month service. The present model also shows that the inner surface is the most vulnerable part of the cladding. Therefore, the inspection should focus on the inner surface of the cladding along its the entire height.

It is evident that one important component of the present model is the kinetics of damage growth (Eq. 2.11). In this kinetics model, the dependence of the damage growth rate on the applied loading is governed by the exponent n in Eq. 2.11. Fig. 5.7a shows a parametric study on how the value of n influences the time evolution of the failure probability. It is seen that with an increasing value of n the failure probability of the entire structure decreases. This is because, as n increases, the damage growth rate decreases and so does the failure probability. Fig. 5.7a also includes the failure probability calculated from the time-independent model. In this model, the overall failure statistics of the cladding is still represented by the weakest-link model (Eq. 5.1), but the failure probability function P_{fs} is calculated solely based on the current stress state using Eq. 2.9. As compared to the present time-dependent model, the key difference is that the time-independent model ignores the damage state of the material and treats the material is in the virgin state for the current loading state. This is an oversimplification, which can cause a gross underestimation of the failure risk. The present model keeps track of the

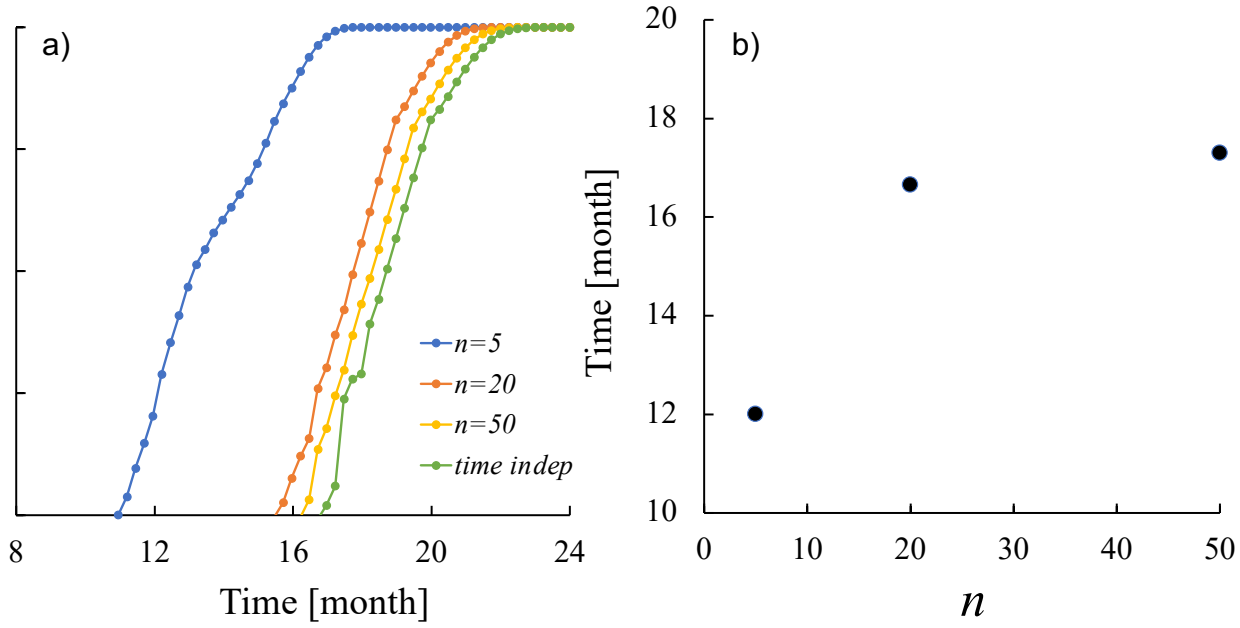

Figure 5.7: (a) Lifetime distributions of cladding calculated by using different n values and a time-independent model, and (b) the corresponding service lifetimes corresponding to $P_f = 10^{-6}$.

damage state through the damage accumulation model, and therefore would predict a higher failure risk than the time-independent model.

Fig. 5.7b shows the lifetime of the cladding for the failure risk of 10^{-6}. It is seen as n-value varies from 50 to 5, the service lifetime of the cladding decreases from 17 months to 12 months. This indicates the significant influence of the n-value on the prediction of the lifetime distribution of the cladding. Therefore, it is crucial to experimentally determine the parameter n. One method is to perform the strength test using a linear ramped loading and the lifetime test using static fatigue on the same batch of specimens. Based on the measured strength and lifetime, Eq. 2.15 can be used to determine the value of n.

5.5 Effect of the Cladding Length to Failure Probability

The actual cladding in LWR is around 4m long, which makes it difficult to perform direct mechanical tests. Therefore, it is customary to test specimens of shorter lengths. The essential question for design is how to extrapolate the laboratory test results to full length design. To facilitate this design extrapolation, we investigate the effect of the cladding length on the failure probability. Since the failure probability is calculated based on the elastic stress analysis, the stress distribution is independent of the cladding length.

Fig. 5.8 presents the calculated failure probability of claddings of different lengths. The failure probability of the cladding increases with the increasing length. At a given time, the failure probability of a cladding of 4 m long could be twice the failure probability of a 1m

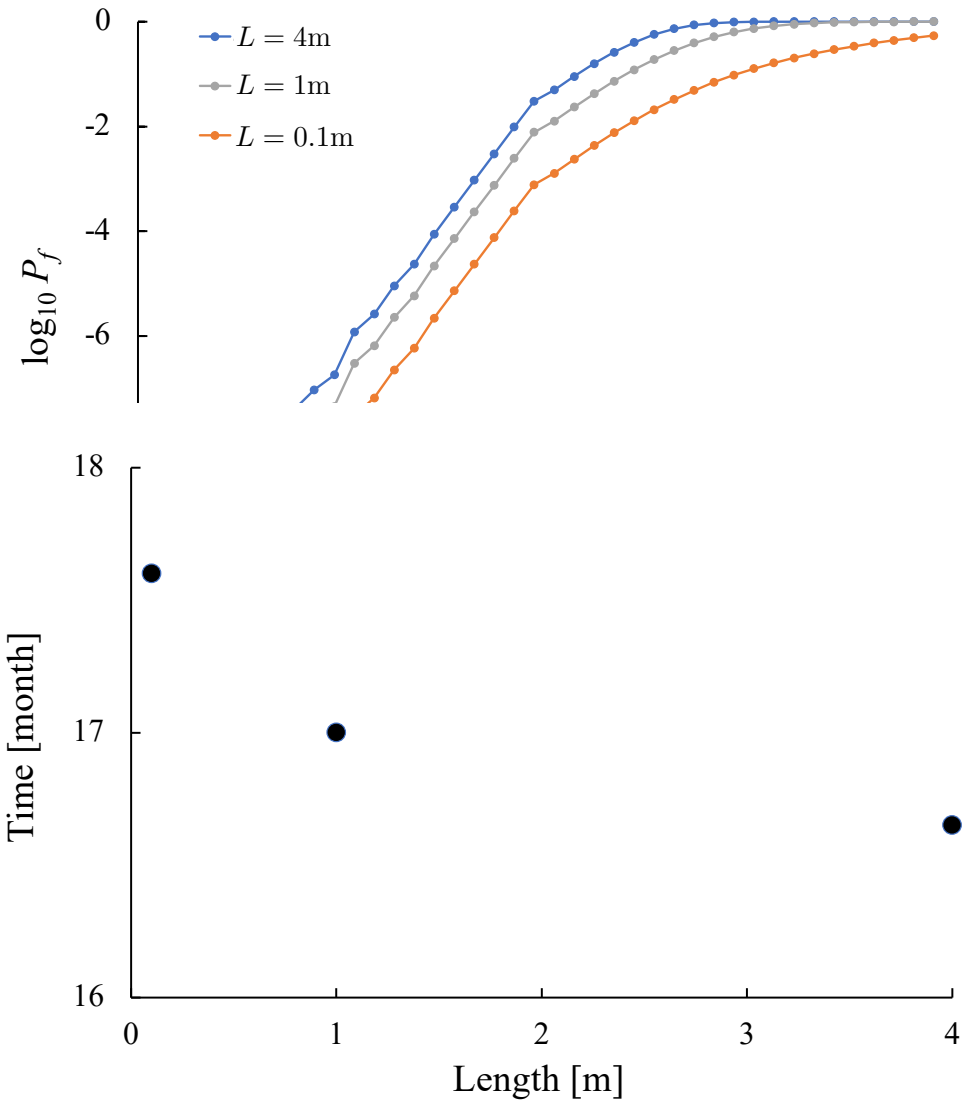

Figure 5.9: Length effect on the service lifetime of the cladding corresponding to $P_f = 10^{-6}$.

cladding. This difference would be much more pronounced if we compare claddings with a larger length ratio. This behavior is due to the fact that the failure of the cladding is governed by the weakest element. Since most of the cladding experiences a uniform stress distribution, a longer cladding would have a large likelihood to contain weaker elements and consequently a higher failure risk. This is a classical feature of the weakest link statistical model.

Fig. 5.9 shows the relationship between the service lifetime corresponding to a failure probability of 10^{-6} and the cladding length. The lifetime of a 4m cladding is 16.7 months while that of a 1m cladding is 17.6 months. This is a strong size effect on the design lifetime, which needs to be taken into consideration in the design extrapolation. The direct consequence of this finding is that the safety factor determined based on the laboratory tests needs to be adjusted for the design of full length structure. Otherwise, the failure probability of the actual structure would be much larger than the tolerable value.

6 Conclusions and Recommendations

6.1 Conclusions

- A multiaxial failure model is proposed for SiC/SiC composites. The failure model is extended to capture the probabilistic behavior. It is shown that, for the stress states of present interest, the probabilistic behavior of the failure surface can be well described for the probability distributions of the proportional limit stresses (PLS) in the axial, hoop, and biaxial directions.

- A robust multiaxial testing systems is developed for generating various load combinations of axial force and internal pressure. To provide the effective isolation (jacketing) from the internal fluid pressure, Viton membranes of a special shape are manufactured to seal both the internal surface of specimen and interface between the specimen and apparatus. High strength epoxy is used in-between the contracted surface of the specimen and apparatus to transmit axial loading. With this design, the system is able to load the specimen up to ultimate failure.

- A new strain-based criterion is proposed for determining the PLS for multiaxial loading. The criterion reduces to the current ASTM recommendation on the PLS for uniaxial tensile loading. The proposed criterion is validated by the comparison with the results of acoustic emission. With the newly designed test apparatus, the multiaxial failure surface corresponding to the PLS with its statistical variation is experimentally measured.

- The time dependence of the failure statistics of SiC/SiC composites is formulated through a damage kinetics model. The damage accumulation mechanism indicates that the failure probability of the material at any given time is governed by the entire previous loading history, a key difference from the time-independent model in which the failure probability depends only on the current stress state.

- It is demonstrated that the damage growth kinetics has a profound influence on the time evolution of failure probability of the cladding. Therefore, to accurately predict the lifetime distribution of the cladding, it is crucial to calibrate the damage growth model for SiC/SiC composites. Based on the present model, it is suggested to use a combination of strength test and static fatigue lifetime test to calibrate the damage kinetics model.

- The failure probability of the SiC/SiC cladding is calculated from the material failure probability through a weakest-link model, which signifies the damage localization mechanism. Since the cladding experiences a relatively uniform stress distribution along its height, the failure probability is strongly dependent on the cladding length. It shown that

a longer cladding would experience a considerably higher failure probability as compared to a shorter one.

6.2 Recommendations

In this study, we define failure of the entire structure to occur once any material element reaches the PLS. This definition is conservative because, in actual application, the cracks initiated at the cladding inner region could be arrested by the compressive stress at outer region. In this case, hermeticity of the system may be retained and the actual failure risk of the cladding would be lower than that calculated by the present model. To capture the behavior of crack propagation for estimating the failure risk, one would need to rely on stochastic numerical simulations (e.g. finite element analysis), which involve a nonlinear constitutive material model with spatially distributed random material properties (e.g. [12]). Such type of numerical models are appealing as they will yield a more accurate estimation of failure risk as well as reveal the cracking pattern at failure. Though the computational cost could be high, full scale nonlinear stochastic computation will be feasible with the advances in modern computing technology. In comparison, the present model provides an efficient means for estimating an upper bound of failure risk while taking into account the effect of damage accumulation.

The finding of the present study indicates the importance of understanding the subcritical damage growth behavior. In nuclear applications, the subcritical damage growth not only deteriorates the load carrying capacity of the structure, but also affects the structural integrity. So far most laboratory experiments focused solely on strength properties. There is a clear need to experimentally investigate the subcritical damage growth under sustained loading combined with other environmental conditions such as high temperatures and irradiation. Such experimental data will allow us to quantify the kinetics of subcritical damage growth, to reveal the underlying mechanisms, and to calibrate the relevant numerical and theoretical models.

The present model reveals the important consequences of the damage accumulation mechanism as well as the size effect for assessing the lifetime distribution of SiC/SiC composite cladding. These findings suggest the critical need of future work on experimental characterization of mechanical behavior of SiC/SiC composite materials as an essential step toward reliability-based design of SiC/SiC composite claddings.

References

[1] Z. P. Bažant. *Scaling of Structural Strength*. Elsevier, London, 2005.

[2] Z. P. Bažant and J.-L. Le. *Probabilistic Mechanics of Quasibrittle Structures: Strength, Lifetime, and Size Effect*. Cambridge University Press, 2017.

[3] Z. P. Bažant, J.-L. Le, and M. Z. Bazant. Scaling of strength and lifetime distributions of quasibrittle structures based on atomistic fracture mechanics. *Proceedings of the National Academy of Sciences*, 106:11484–11489, 2009.

[4] Z. P. Bažant and J. Planas. *Fracture and Size Effect in Concrete and Other Quasibrittle Materials*. CRC Press, Boca Raton, 1998.

[5] Z. P. Bažant and S.-D. Pang. Activation energy based extreme value statistics and size effect in brittle and quasibrittle fracture. *Journal of the Mechanics and Physics of Solids*, 55(1):91–131, 2007.

[6] M. Ben-Belgacem, V. Richet, K.A. Terrani, Y. Katoh, and L.L. Snead. Thermo-mechanical analysis of LWR SiC/SiC composite cladding. *Journal of Nuclear Materials*, 447(1):125 – 142, 2014.

[7] F. Bernachy-Barbe, L. Gélébart, M. Bornert, J. Crépin, and C. Sauder. Anisotropic damage behavior of SiC/SiC composite tubes: Multiaxial testing and damage characterization. *Composites Part A: Applied Science and Manufacturing*, 76:281 – 288, 2015.

[8] C.P. Deck, G.M. Jacobsen, J. Sheeder, O. Gutierrez, J. Zhang, J. Stone, H.E. Khalifa, and C.A. Back. Characterization of SiC–SiC composites for accident tolerant fuel cladding. *Journal of Nuclear Materials*, 466:667 – 681, 2015.

[9] Y. Deng, K. Shirvan, Y. Wu, and G. Su. Probabilistic view of SiC/SiC composite cladding failure based on full core thermo-mechanical response. *Journal of Nuclear Materials*, 507:24–37, 2018.

[10] R. A. Fisher and L. H. C. Tippet. Limiting form of the frequency distribution the largest and smallest number of a sample. *Proc. Cambridge. Philos. Soc.*, 24:180–190, 1928.

[11] A. M. Freudenthal. Statistical approach to brittle fracture. In *Fracture: An Advanced Treatise, vol. 2*, pages 591–619, New York, 1968.

[12] A. Gorgogianni, J. Eliáš, and J.-L. Le. Mesh objective stochastic simulations of quasibrittle fracture. *J. Mech. Phys. Solids*, 159:104745, 2022.

[13] A. Haldar and S. Mahadevan. *Probability, Reliability, and Statistical Methods in Engineering Design*. Wiley, New York, 2000.

[14] L. Kachanov. *Introduction to continuum damage mechanics*. Springer Netherlands, Dordrecht, 1986.

[15] M. Kachanov. On the concept of damage in creep and in the brittle-elastic range. *Int J Damage Mech*, 3:329–337, 10 1994.

[16] Y. Katoh, K. Ozawa, C. Shih, T. Nozawa, R. J. Shinavski, A. Hasegawa, and L. L. Snead. Continuous SiC fiber, CVI SiC matrix composites for nuclear applications: Properties and irradiation effects. *Journal of Nuclear Materials*, 448(1-3):448–476, May 2014.

[17] D. Kim, H.-G. Lee, J. Y. Park, and W.-J. Kim. Fabrication and measurement of hoop strength of SiC triplex tube for nuclear fuel cladding applications. *Journal of Nuclear Materials*, 458:29 – 36, 2015.

[18] J. Lamon. *Chemical Vapor Infiltrated SiC/SiC Composites (CVI SiC/SiC)*, pages 55–76. Springer US, Boston, MA, 2005.

[19] J.-L. Le. Size effect on reliability indices and safety factors of quasibrittle structures. *Structural Safety*, 52:20–28, 2015.

[20] J.-L. Le and Z. P. Bažant. Strength distribution of dental restorative ceramics: Finite weakest link model with zero threshold. *Dental Materials*, 25(5):641–648, 2009.

[21] J.-L. Le, Z. P. Bažant, and M. Z. Bazant. Unified nano-mechanics based probabilistic theory of quasibrittle and brittle structures: I. strength, static crack growth, lifetime and scaling. *Journal of the Mechanics and Physics of Solids*, 59(7):1291–1321, 2011.

[22] T. Nozawa, S. Kim, K. Ozawa, and H. Tanigawa. Stress envelope of silicon carbide composites at elevated temperatures. *Fusion Engineering and Design*, 89(7):1723–1727, 2014.

[23] Y. N. Rabotnov. *Creep Problem in Structural Members*. North-Holland, Amsterdam, 1969.

[24] E. Rohmer, E. Martin, and C. Lorrette. Mechanical properties of SiC/SiC braided tubes for fuel cladding. *Journal of Nuclear Materials*, 453(1):16 – 21, 2014.

[25] L. Saucedo-Mora, T. Lowe, S. Zhao, P.D. Lee, P.M. Mummery, and T.J. Marrow. In situ observation of mechanical damage within a SiC-SiC ceramic matrix composite. *Journal of Nuclear Materials*, 481:13–23, 2016.

[26] K. Shapovalov, G. M. Jacobsen, L. Alva, N. Truesdale, C. P. Deck, and X. Huang. Strength of SiC_f-SiC_m composite tube under uniaxial and multiaxial loading. *Journal of Nuclear Materials*, 500:280 – 294, 2018.

[27] G. Singh, S. Gonczy, C. Deck, E. Lara-Curzio, and Y. Katoh. Interlaboratory round robin study on axial tensile properties of SiC-SiC CMC tubular test specimens. *International Journal of Applied Ceramic Technology*, 15(6):1334–1349, 2018.

[28] G. Singh, K. Terrani, and Y. Katoh. Thermo-mechanical assessment of full SiC/SiC composite cladding for LWR applications with sensitivity analysis. *Journal of Nuclear Materials*, 499:126 – 143, 2018.

[29] J.G. Stone, R. Schleicher, C.P. Deck, G.M. Jacobsen, H.E. Khalifa, and C.A. Back. Stress analysis and probabilistic assessment of multi-layer SiC-based accident tolerant nuclear fuel cladding. *Journal of Nuclear Materials*, 466:682–697, 2015.

[30] K. A. Terrani, B. A. Pint, C. M Parish, C. M. Silva, L. L. Snead, and Y. Katoh. Silicon carbide oxidation in steam up to 2 MPa. *Journal of the American Ceramic Society*, 97(8):2331–2352, 2014.

[31] Kurt A. Terrani. Accident tolerant fuel cladding development: Promise, status, and challenges. *Journal of Nuclear Materials*, 501:13–30, 2018.

[32] E. Vanmarcke. *Random Fields Analysis and Synthesis*. World Scientific Publishers, Singapore, 2010.

[33] W. Weibull. The phenomenon of rupture in solids. *Proc. Royal Sweden Inst. Engrg. Res.*, 153:1–55, 1939.

[34] W. Weibull. A statistical distribution function of wide applicability. *Journal of Applied Mechanics*, 153(18):293–297, 1951.